Interseismic coupling and seismic potential along the Central Andes subduction zone

Mohamed Chlieh, Hugo Perfettini, Hernando Tavera, Jean-Philippe Avouac, Dominique Remy, Jean-Mathieu Nocquet, Frédérique Rolandone, Francis Bondoux, Germinal Gabalda, Sylvain Bonvalot

Interseismic coupling and seismic potential along the Central Andes subduction zone

Mohamed Chlieh,[1] Hugo Perfettini,[2] Hernando Tavera,[3] Jean-Philippe Avouac,[4] Dominique Remy,[5] Jean-Mathieu Nocquet,[1] Frédérique Rolandone,[6] Francis Bondoux,[5] Germinal Gabalda,[5] and Sylvain Bonvalot[5]

Received 16 December 2010; revised 10 September 2011; accepted 3 October 2011; published 17 December 2011.

[1] We use about two decades of geodetic measurements to characterize interseismic strain build up along the Central Andes subduction zone from Lima, Peru, to Antofagasta, Chile. These measurements are modeled assuming a 3-plate model (Nazca, Andean sliver and South America Craton) and spatially varying interseismic coupling (ISC) on the Nazca megathrust interface. We also determine slip models of the 1996 M_w = 7.7 Nazca, the 2001 M_w = 8.4 Arequipa, the 2007 M_w = 8.0 Pisco and the M_w = 7.7 Tocopilla earthquakes. We find that the data require a highly heterogeneous ISC pattern and that, overall, areas with large seismic slip coincide with areas which remain locked in the interseismic period (with high ISC). Offshore Lima where the ISC is high, a M_w∼8.6–8.8 earthquake occurred in 1746. This area ruptured again in a sequence of four M_w∼8.0 earthquakes in 1940, 1966, 1974 and 2007 but these events released only a small fraction of the elastic strain which has built up since 1746 so that enough elastic strain might be available there to generate a $M_w > 8.5$ earthquake. The region where the Nazca ridge subducts appears to be mostly creeping aseismically in the interseismic period (low ISC) and seems to act as a permanent barrier as no large earthquake ruptured through it in the last 500 years. In southern Peru, ISC is relatively high and the deficit of moment accumulated since the M_w∼8.8 earthquake of 1868 is equivalent to a magnitude M_w∼8.4 earthquake. Two asperities separated by a subtle aseismic creeping patch are revealed there. This aseismic patch may arrest some rupture as happened during the 2001 Arequipa earthquake, but the larger earthquakes of 1604 and 1868 were able to rupture through it. In northern Chile, ISC is very high and the rupture of the 2007 Tocopilla earthquake has released only 4% of the elastic strain that has accumulated since 1877. The deficit of moment which has accumulated there is equivalent to a magnitude M_w∼8.7 earthquake. This study thus provides elements to assess the location, size and magnitude of future large megathurst earthquakes in the Central Andes subduction zone. Caveats of this study are that interseismic strain of the forearc is assumed time invariant and entirely elastic. Also a major source of uncertainty is due to fact that the available data place very little constraints on interseismic coupling at shallow depth near the trench, except offshore Lima where sea bottom geodetic measurements have been collected suggesting strong coupling.

Citation: Chlieh, M., H. Perfettini, H. Tavera, J.-P. Avouac, D. Remy, J.-M. Nocquet, F. Rolandone, F. Bondoux, G. Gabalda, and S. Bonvalot (2011), Interseismic coupling and seismic potential along the Central Andes subduction zone, *J. Geophys. Res.*, *116*, B12405, doi:10.1029/2010JB008166.

1. Introduction

[2] With the development of the Global Positioning System (GPS) and Synthetic Aperture Radar interferometry (InSAR), it is now possible to measure very precisely surface displacements associated with both interseismic strain build up and co-seismic strain release along plate boundaries. Several subduction zones have been studied using this approach including Sumatra, Japan, New Zeeland, Kamchatka, Alaska, Cascadia, Mexico, Chile and Peru [*Bürgmann et al.*,

[1]Géoazur, IRD UR 082, CNRS UMR 6526, Université de Nice Sophia-Antipolis, Observatoire de la Côte d'Azur, Valbonne, France.
[2]Institut des Sciences de la Terre, IRD UR 219, CNRS UMR 5275, Université Joseph Fourier, Observatoire des Sciences de l'Univers de Grenoble, Grenoble, France.
[3]Instituto Geofisico del Peru, Lima, Peru.
[4]Tectonics Observatory, California Institute of Technology, Pasadena, California, USA.
[5]Géosciences Environnement Toulouse, IRD UR 234, CNRS UMR 5563, Université de Toulouse, Observatoire Midi-Pyrénées, Toulouse, France.
[6]Institut des Sciences de la Terre de Paris, CNRS UMR 7193, Université Pierre et Marie Curie, Paris, France.

0148-0227/11/2010JB008166

2005; *Chlieh et al.*, 2004; *Freymueller et al.*, 2000; *Khazaradze and Klotz*, 2003; *Loveless and Meade*, 2010; *Moreno et al.*, 2010; *Perfettini et al.*, 2010; *Wallace et al.*, 2004; *Wang et al.*, 2003; *Yoshioka et al.*, 2004]. In all these examples, heterogeneous interseismic strain has been revealed suggesting that the plate interface in the 0–40 km seismogenic depth range consists of interfingered patches that either remain locked or creep aseismically. This patchwork is generally characterized from the pattern of interseismic coupling (ISC), defined as the ratio of the slip deficit rate and the long-term slip rate. Consequently, an ISC value of 1 corresponds to full locking while an ISC of 0 corresponds to creeping at the long-term plate convergence rate. In addition, most of these studies suggest that seismic slip during large interplate earthquakes tends to occur in areas that remain locked in the interseismic period, and that the rupture tends not to propagate into interseismically creeping areas [*Bürgmann et al.*, 2005; *Chlieh et al.*, 2008; *Hashimoto et al.*, 2009; *Konca et al.*, 2008; *Moreno et al.*, 2010; *Perfettini et al.*, 2010; *Yoshioka et al.*, 2004]. It follows that the fault zones with relatively high or low co-seismic slip, respectively called asperities and barriers, are to some degree related to the pattern of interseismic coupling and might be persistent features. This persistence might explain the proposed correlation between the locations of seismic asperities and various geometrical features or long-term deformation of the forearc [*Audin et al.*, 2008; *Collot et al.*, 2004; *Llenos and McGuire*, 2007; *Loveless et al.*, 2009; *Sladen et al.*, 2010; *Song and Simons*, 2003; *Wells et al.*, 2003]. The persistence can also be interpreted using the rate-and-state friction theory [e.g., *Scholz*, 1998]: the locked patches presumably obey a rate-weakening behavior, while the creeping patches are presumably rate-strengthening. Dynamic modeling has shown that the rate-strengthening patches can indeed systematically arrest seismic rupture, and appear as permanent barriers, while rate-weakening patches tend to remain locked or slip in transient events [*Kaneko et al.*, 2010]. Transient slip events can take the form of earthquakes followed by aseismic afterslip, generally around the seismic asperities [*Barrientos et al.*, 1992; *Brown et al.*, 1977; *Chlieh et al.*, 2004; *Heki and Tamura*, 1997; *Hsu et al.*, 2006; *Perfettini et al.*, 2010], or aseismic slip events, which may occur spontaneously [*Dragert et al.*, 2001; *Hirose et al.*, 1999; *Lowry et al.*, 2001; *Miyazaki et al.*, 2003], or triggered by a seismic event [*Pritchard and Simons*, 2006]. All modes of aseismic slip, whether related to afterslip or slow slip events can be modeled in the framework of rate-and-state friction [*Liu and Rice*, 2007; *Perfettini and Avouac*, 2004; *Perfettini and Ampuero*, 2008].

[3] Therefore, it is instructive to determine the pattern of ISC on a megathrust fault and compare the cumulative rate of moment deficit in the interseismic period with the moment released by former earthquakes. Such a comparison is the purpose of this study. Here, we focus on the subduction zone offshore of northern Chile and southern Peru where four $M_w \geq 7.7$ subduction earthquakes occurred between 1996 and 2007 that are, the 1996 Nazca $M_w = 7.7$, the 2001 Arequipa $M_w = 8.4$, the 2007 Pisco $M_w = 8.0$ and the Tocopilla $M_w = 7.7$ earthquakes (Figure 1). Larger earthquakes, with moment magnitudes $M_w > 8.5$ have occurred in 1746, 1868 and 1877 [*Dorbath et al.*, 1990; *Silgado*, 1978]. A long time has elapsed since these larger events, such that elastic strain is expected to have built up to a level, which could allow similar events to occur in the near future. Our analysis provides insights into the elastic strain available for future earthquake and might be useful in forecasting rupture scenarios [*Kaneko et al.*, 2010]. One caveat of our study worth pointing out upfront is that interseismic strain is determined from geodetic data acquired over a period of about a decade, which is too short to be representative of the full interseismic period. It is known that strain rates can significantly vary over the interseismic period as observed following the great earthquakes of Chile ($M_w = 9.5$, 1960) or Alaska ($M_w = 9.2$, 1964) [*Freymueller et al.*, 2000; *Khazaradze et al.*, 2002]. Models which take into account viscous flow in depth do indeed predict a non-stationary interseismic deformation [*Hu et al.*, 2004; *Johnson and Segall*, 2004; *Perfettini and Avouac*, 2004] and a broader zone of elastic strain accumulation which is predicted by purely elastic models [*Wang et al.*, 2007]. A full account of these effects is difficult given the limited data. In this work, we partially address some of these issues by considering possible loading rate variations in the interseismic period. Another caveat is that all of the interseismic strain of the forearc measured from geodesy is assumed to represent elastic strain to be released by seismic slip along the Megathrust. This assumption is justified by the limited long-term deformation of the forearc that is probably incorrect at places, especially around most peninsulas [*Collot et al.*, 2004; *Melnick et al.*, 2009; *Victor et al.*, 2011].

[4] In this paper, we examine geodetic measurements of both interseismic and coseismic deformation along the seismically active Peru-Chile subduction megathrust. We analyze interseismic geodetic measurements (GPS and InSAR) recorded in a ten-year period prior to the four 1996–2007 $M_w > 7.7$ subduction earthquakes. Then, we determine the distribution of interseismic coupling on the megathrust interface and the associated rate of moment deficit. In order to compare that interseismic coupling with subsequent major megathrust earthquakes, we also determine the source distributions of these four earthquakes (Table 1) and their moment released during the coseismic phase and early postseismic phase. To balance the moment budget over the seismic cycle, we integrate the rate of moment deficit and compare it to the seismic moment released by recent and historical large earthquakes. Based on this analysis we propose maximum and minimum bounds of the seismic potential along the subduction megathrust from the megapolis of Lima in central Peru to the coastal city of Antofagasta in northern Chile.

2. Seismotectonic Context

[5] The Nazca plate rotates anti-clockwise relative to the South American Craton at an angular rate of 0.57°/Myr around a pole located in North America at 94.4°W and 61.0°N [*Kendrick et al.*, 2003]. As a consequence, the velocity of the Nazca plate relative to South America along the trench increases from 61.7 mm/a at latitude 14°S to 63.3 mm/a at latitude 24°S (Figure 2). These velocities are about 20% slower and have an azimuth shifted about 5°N clockwise compared to the velocities predicted by the Nuvel-1A global plate model [*DeMets et al.*, 1994]. Other studies based on IGS GPS stations [*Altamimi et al.*, 2002; *Sella et al.*, 2002]

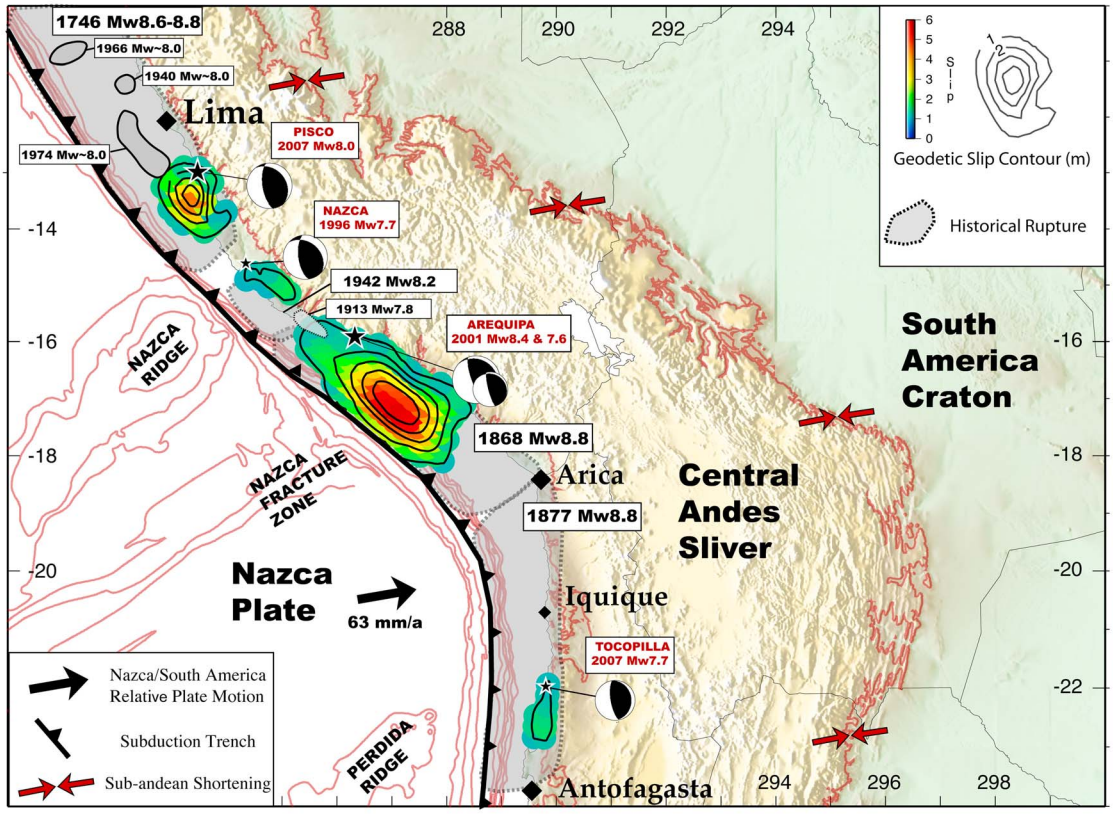

Figure 1. Seismotectonic setting of the Central Andes subduction zone with rupture of large ($M_w > 7.5$) subduction earthquakes on the Peru-Chile megathrust since 1746. The Central Andes sliver is squeezed between the Nazca plate and the South America Craton. Convergence rate of the Nazca plate relative to the South America Craton (black arrow) is computed from *Kendrick et al.* [2003]. Shortening across the Subandean foothills is represented with the red arrows (assumed parallel to the Nazca/South America plate convergence). Red contours are the 1000 m of the Andes topography and the −5000 m to −3000 m bathymetric contour lines. Historical ruptures are compiled from *Beck and Ruff* [1989] and *Dorbath et al.* [1990]. Slip distributions of the 2007 M_w = 8.0 Pisco, 1996 M_w = 7.7 Nazca, 2001 M_w = 8.4 Arequipa and 2007 M_w = 7.7 Tocopilla earthquakes were determined from joint inversions of the InSAR and GPS data (this study). These source models include coseismic and afterslip over a few weeks to a few months depending on case. Slip contours are reported each 1-m. The color scale indicates slip amplitude.

propose a slightly different pole location but the relative plates convergence rates are within 3% of those of determined based on *Kendrick et al.* [2003]. *Vigny et al.* [2009] found a different pole and angular velocity (Long. 95.2°W, Lat. 55.9°N, and ω = 0.61°/Ma) implying a slightly higher convergence rate of 68 mm/a in the Central Andes [*Vigny et al.*, 2009]. Although more GPS sites would be needed to better constrain the Nazca plate motion relative to South America, the solution of *Kendrick et al.* [2003], which includes additional sites on the Nazca plate, is probably the most reliable solution for the purpose of this study.

[6] Shortening in the sub-Andean regions has been well documented from geological and paleomagnetic reconstructions of the Central Andes [*Arriagada et al.*, 2008; *Baby et al.*, 1993, 1997; *Barke et al.*, 2007; *Kley and Monaldi*, 1998; *Lamb*, 2000; *McQuarrie et al.*, 2008; *Oncken et al.*, 2006].

Table 1. Harvard Centroid Moment Tensor Associated With the M_w = 7.7 Nazca, the M_w = 8.4 Arequipa and Its M_w = 7.6 Aftershock, the M_w = 8.0 Pisco and the M_w = 7.7 Tocopilla Earthquakes[a]

Date	Name	M_w	Long.	Lat.	Strike	Dip	Rake	Seismic Moment (10^{21} Nm)	Geodetic Moment (10^{21} Nm)
11/12/96	Nazca,	7.7	−75.37	−15.04	312	33	55	0.45	0.53
06/23/01	Arequipa	8.4	−72.71	−17.28	310	18	63	4.67	5.20
07/07/01	Aftersh.	7.6	−72.45	−17.45	306	14	52	0.32	5.20
08/15/07	Pisco	8.0	−77.04	−13.73	321	28	63	1.11	1.50
11/14/07	Tocopilla	7.7	−70.62	−22.64	358	20	98	0.47	0.67

[a]Columns 4 and 5 are the coordinates and columns 6, 7 and 8 report respectively the strike, the dip and the rake of the first nodal plan. The seismic moments are reported in column 9 and the geodetic moment issue from this study in column 10. The geodetic moment reported for Arequipa include the moment of the M_w = 8.4 and of its M_w = 7.6 aftershock and should be compared to the seismic moments summation of these two events.

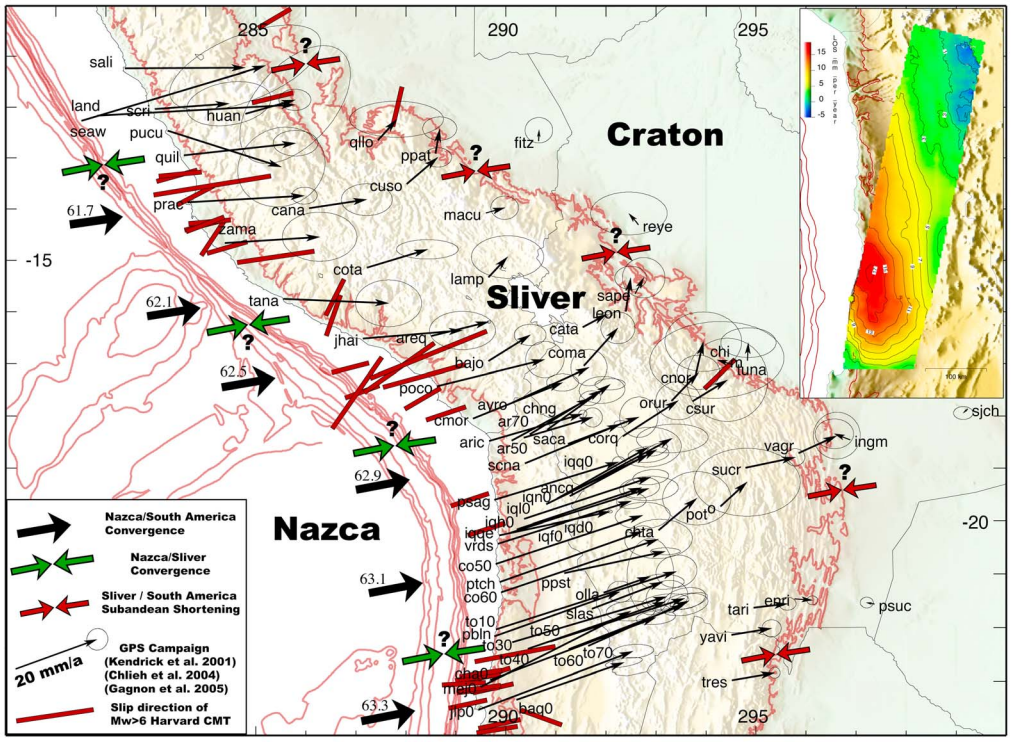

Figure 2. Interseismic geodetic measurements in the Central Andes subduction zone. Horizontal velocities determined from campaign GPS measurements are shown relative to South America Craton. Inset shows unwrapped interseismic interferogram in mm/a projected in the line of sight (LOS) direction of the ERS-1/2 satellites [*Chlieh et al.*, 2004]. The convergence of the Nazca plate relative to South America (black arrows) is mainly accommodated along the Peru-Chile megathrust (green arrows) with a fraction taken up along the subandean fold and thrust belt (red arrows). Red bars represent the slip direction of $M_w > 6$ Harvard CMT (http://www.seismology.harvard.edu/CMTsearch.html).

Although the total amount of shortening is still debated, most studies agree that mid-Neogene to present deformation is mainly localized in the sub-Andean zone. Plio-Quaternary geological shortening rates of the order of 10 mm/a to 15 mm/a are estimated in the Central Andes [*Hindle et al.*, 2002]. Geodetic studies have reported slower rates of shortening of about 4 mm/a to 9 mm/a west of the Altiplano plateau [*Bevis et al.*, 2001; *Chlieh et al.*, 2004; *Khazaradze and Klotz*, 2003].

[7] *Silgado* [1978] and later *Dorbath et al.* [1990] have analyzed the information available on large historical earthquakes along the coast of Peru since the arrival of the conquistadores in the 16th century. These studies provide estimates of the rupture areas and moment magnitude, M_w, of these large earthquakes. The Peruvian subduction can be divided into three distinct zones separated by two prominent geomorphologic features on the subducting plate: the Mendaña fracture zone at latitudes of 10°S and the Nazca ridge at 15°S.

[8] In the central zone (between the Mendaña fracture zone and the Nazca ridge), the great 1746 megathrust earthquake ruptured the entire zone and Lima's port Callao was devastated by a tsunami with only a few hundreds out of 6000 people surviving [*Walker*, 2008]. *Dorbath et al.* [1990] estimated the magnitude of this event to be of the order of M_w∼8.6, but *Beck and Nishenko* [1990] suggested a larger value of M_w∼8.8 to 9.5. In the following we consider for that event a moment magnitude range of M_w∼8.6–8.8. The 1746 great earthquake was followed by two centuries of seismic quiescence, interrupted in the 20th century by the occurrence of three M_w∼8.0 earthquakes: the 1940 event followed by the 1966 and 1974 earthquakes [*Beck and Ruff*, 1989; *Beck and Nishenko*, 1990; *Langer and Spence*, 1995]. The M_w = 8.0 Pisco earthquake of 2007 whose rupture stopped at the northern edge of the Nazca ridge, completed the sequence to spatially encompass approximately the whole rupture area of the great 1746 earthquake [*Audin et al.*, 2007; *Biggs et al.*, 2009; *Motagh et al.*, 2008; *Perfettini et al.*, 2010; *Pritchard and Fielding*, 2008; *Sladen et al.*, 2010; *Tavera and Bernal*, 2008].

[9] The southern zone, located between the Nazca ridge and the Arica bend (Chilean border) is the site of the largest earthquakes in Peru (Figure 1). Repeated large earthquakes are reported to have occurred there since the 16th century with an average recurrence time of the order of 130 years for $M_w \geq 8.4$ earthquakes. It seems that no historical event ever ruptured the segment where the Nazca ridge subducts suggesting that this area is a permanent barrier to earthquakes rupture propagation. Just south of the Nazca ridge, the 1942 M_w∼8.1–8.2 earthquake ruptured about 150 km southwards. The M_w = 7.7 Nazca earthquake in 1996 seems to have broken only a small portion deeper than the 1942 rupture. The last great earthquake in southern Peru occurred in 1868 with the tsunamigenic M_w∼8.8 event which has ruptured

about 450 km of the southern Peruvian megathrust. The M_w = 8.4 Arequipa earthquake in 2001 reactivated the northern portion of the 1868 rupture, leaving the southern segment unbroken. The rupture propagated southwards over 300 km and stopped near the Ilo Peninsula [*Audin et al.*, 2008]. Seismological studies of the 1996 and 2001 earthquakes indicate unilateral ruptures toward the southeast and multipeaked source time functions [*Giovanni et al.*, 2002; *Pritchard et al.*, 2007; *Robinson et al.*, 2006; *Salichon et al.*, 2003; *Swenson and Beck*, 1999]. In the north of the Mejillones Peninsula in Chile, the last M_w > 8.0 subduction event is the great tsunamigenic earthquake of 1877 M_w∼8.5–8.8 which damaged Chile, Peru and many coastal areas around the Pacific. The 2007 M_w = 7.7 Tocopilla earthquake has characteristics similar to the 1996 Nazca event in the sense that it ruptured only the deeper portion of the seismogenic zone, releasing only a tiny fraction of the seismic moment released by the previous great earthquakes [*Béjar-Pizarro et al.*, 2010; *Peyrat et al.*, 2010].

3. GPS and InSAR Data

3.1. Interseismic Survey-Mode GPS and Permanent GPS

[10] We use velocities from 87 sites surveyed during GPS campaigns from 1993 to 2003 [*Chlieh et al.*, 2004; *Gagnon et al.*, 2005; *Kendrick et al.*, 2001]. These survey-mode GPS data cover an area that extends along the coast from Lima region (Lat. 11°S) in central Peru to the Mejillones Peninsula in northern Chile (Lat. 24°S). Inland, this data set covers all southern Peru, northern Chile, the Altiplano plateau, Bolivia and Argentina (Figure 2). *Kendrick et al.* [2001] proposed an integrated crustal velocity field including the GPS campaigns of both the South America-Nazca Plate Project (SNAPP) and the Central Andes GPS Project (CAP) [*Bevis et al.*, 1999; *Norabuena et al.*, 1998]. We reprocessed the data from the CAP project for southern Peru, available at UNAVCO facility (http://facility.unavco.org/data/gnss/campaign.php). We found less than 1 mm/a of differences with respect to the values published by *Kendrick et al.* [2001]. We selected 56 GPS measurements from the study of *Kendrick et al.* [2001]. We added 5 GPS measurements on- and off- shore the city of Lima [*Gagnon et al.*, 2005]. Finally we completed our velocity field with 26 GPS measurements in northern Chile published by *Chlieh et al.* [2004]. Some of these data were processed in ITRF97 and others in ITRF2000, with possible slightly different realizations of the Stable South-America plate. All the data were incorporated in a single consistent velocity field using the method described by *Aktug et al.* [2009]. We estimate a rotation rate vector for each individual solution and imposed the rotation rate between the resulting combined solution and the solution from *Kendrick et al.* [2001] to be null. Individual variance for each individual solution is rescaled until both individual and overall a posteriori variance factor equals 1 in the combination [*Aktug et al.*, 2009]. The combined interseismic GPS velocities are listed with their 1-sigma uncertainties in the geodetic section in the auxiliary material.[1]

[1]Auxiliary materials are available in the HTML. doi:10.1029/2010JB008166.

3.2. Interseismic InSAR Data

[11] We used an exceptionally coherent ERS interferogram mapping interseismic deformation between 1995 and 1999 in northern Chile and covering an area of about 500 km × 100 km. The processing of these InSAR measurements is fully described by *Chlieh et al.* [2004]. We unwrapped the interferogram and divided it by the time span between the two image acquisitions to convert it into an interseismic velocity field in the Line of Sight (LOS) of the satellite and the ground. This LOS velocity field appears to be relatively cylindrical and parallel to the trench and the coastal Cordillera. It reaches a maximum of about 17 mm/a near the coast, which is about 100 km from the trench, and decays eastward to less than 2 mm/a at about 150 km inland (inset in Figure 2). The LOS velocity probably reflects the combined effect of both uplift above the downdip end of the locked fault zone and eastward displacement of the forearc margin due to the interplate coupling as discussed by *Chlieh et al.* [2004].

3.3. Co- and Post-Seismic Geodetic Data

[12] To characterize transient slip on the megathrust due to earthquakes and afterslip we used radar images acquired between 1992 and 2007 by the European remote sensing C-band satellites Envisat and ERS-1&2. All images were acquired on various descending tracks covering the areas affected by the four major earthquakes between 1996 and 2007. We process the radar images with the Differential Interferometric Automated Process Applied to Survey Of Nature (DIAPASON) software developed by the Centre National d'Etudes Spatiales (CNES) used for the study of Landers earthquake [*Massonnet et al.*, 1993]. Topographic fringes were corrected using the SRTM digital elevation model [*Farr and Kobrick*, 2000]. We also used the precise orbits determined by Delft Institute for Earth-oriented Space Research (DEOS) for the satellites ERS-1&2 and Envisat (http://www.deos.tudelft.nl/ers/precorbs/orbits/). The interferograms were filtered using an adaptive power-spectrum filter and unwrapped with the Snaphu software [*Chen and Zebker*, 2001]. Finally, we selected ∼100 InSAR observations by subsampling the interferogram. We completed the InSAR measurements of each earthquake with the published GPS measurements when available [*Béjar-Pizarro et al.*, 2010; *Pritchard et al.*, 2007]. All the coseismic geodetic used for this study are listed in the auxiliary material.

4. Interseismic Coupling Modeling

[13] We used the so-called 'back slip' approach [*Savage*, 1983] assuming a uniformly dipping megathrust geometry embedded in a 1-D layered Earth structure from Crust2.0 model. The characteristics of this layered elastic half-space are reported in Table 2. This model assumes that the hanging wall does not deform over the long-term and applies only in the case of planar fault, but it remains a valid approximation even if the megathrust is not strictly planar in reality [*Kanda and Simons*, 2010; *Vergne et al.*, 2001]. The green functions are computed based on the reflectivity method of *Haskell* [1964] following the implementation of *Xie and Yao* [1989] to compute the static displacement field [*Haskell*, 1964; *Xie and Yao*, 1989]. The megathrust geometry is defined by three rectangles of 700 km long each, with the updip edge

Table 2. Earth Structure From Crust2.0 Model for the First 70 km of the Lithosphere [*Bassin et al.*, 2000][a]

Thickness (km)	Vp (km/s)	Vs (km/s)	Density (kg/m^3)	Rigidity (GPa)
0.5	2.5	1.2	2.1	3.02
0.5	4.0	2.1	2.4	10.58
21	6.0	3.5	2.7	33.07
24	6.4	3.7	2.85	39.01
24	7.1	3.9	3.1	47.15

[a]The average rigidity is ~39 GPa.

being consistent with the trench location based on ETOPO2 bathymetry (Table 3). Sensitivity tests for the megathrust dip were run (Table S1 in the auxiliary material). For each segment, we vary the dip from 5° to 21° and calculate separately the residuals associated with the data of northern Chile (South of 19°S), southern Peru (between latitudes 17°S and 19°S) or central Peru (North of 17°S). These tests indicate that the best fitting dip angle is 18° for the northern Chile, 20° for the southern Peru, and 15° for the central Peru segment. For each segment, the optimal inferred dip is consistent with the dip angle of the Harvard focal mechanisms of interplate earthquakes as well as with the locations of relocated hypocenters from the International Seismological Center catalog between 1964 and 1998 [e.g., *Engdhal et al.*, 1998] (Figure S1 in the auxiliary material).

[14] We quantify the misfit between the observations and model predictions using a weighted root mean square of the residuals (wrms) criterion defined as:

$$wrms = \sqrt{\frac{\sum_{i=1,N} \frac{(obs_i - pred_i)^2}{(\sigma_i)^2}}{\sum_{i=1,N} \frac{1}{(\sigma_i)^2}}} \quad (1)$$

where N is the number of observations, (obs_i-$pred_i$) and σ_i are respectively the residual and the uncertainty assigned to the ith velocity component.

4.1. Uniform Locked Fault Zone Models

[15] We first carried out forward models assuming a binary model of coupling and neglecting lateral variations. We consider a locked fault zone (LFZ), which is uniform along-strike with a coupling set to 1 (fully coupled). We selected seven representative models with uniform LFZ extending from 5 km depth at the trench axis to a downdip limit varying in depth from 10 km to 70 km. This corresponds to LFZ widths ranging from about 20 km to 200 km. The slip vector on the megathrust is constrained to be parallel to the average slip vector of Harvard CMT of major megathrust earthquakes. We equally weighted the InSAR observations for the inversion by assigning them 1 cm uncertainty and the GPS measurements were weighted by their assigned uncertainties that are listed in the auxiliary material.

[16] The minimum wrms, when all the geodetic data are taken into account, is reached for the model where the LFZ extent from the trench to 44 km depth (model LFZ44, Table 4). This value is in good agreement with the seismogenic depth range of 45 ± 5 km derived from seismological studies [*Comte et al.*, 1994; *Tichelaar and Ruff*, 1991]. The residuals velocities of model LFZ44 reveal velocities pointing toward the trench in the region where the Nazca ridge subducts and near the Arica corner (Figure S2 in the auxiliary material). This suggests that the interseismic coupling of model LFZ44 is significantly over-estimated there. Also, if we consider regional subset of GPS data corresponding to northern Chile, southern Peru or central Peru, the best fitting model parameters are somewhat different (Table 4). These tests indicate that interseismic coupling may vary along strike.

4.2. Inversion for Heterogeneous ISC, Method

[17] To invert interseismic geodetic measurements for the pattern of ISC, we use the inversion procedure developed by *Ji et al.* [2002]. Each rectangle defined in Table 3 is subdivided into cells of 20 km × 20 km dislocation surfaces. The slip amplitude and the rake are the two parameters to be inverted for each cell. We impose the slip direction not to deviate more than ±20° from the rake reported by the local focal mechanisms. In each cell, the coefficient of coupling is allowed to vary from 0 to 1 with incremental steps of 0.1. The inversion is nonlinear and based on a stochastic simulated annealing algorithm [*Ji et al.*, 2002]. It involves minimizing a cost function defined as the summation of the weighted sum-of-residuals squared and a term meant to control the smoothness of the slip distribution:

$$\text{Cost} = \chi^2 + \lambda \text{Dc}^2 \quad (2)$$

where χ^2 is the chi-square statistic, the coefficient λ modulates the smoothness of the solution and Dc is the average difference of coupling (or seismic slip in case of an earthquake) between adjacent cells. The minimization of the Laplacian is introduced to smooth the inversion. We present in Table S2 and Figure S3 in the auxiliary material sensitivity tests that lead us to fix λ to 0.5 in the following.

[18] We started our inversion models by running several spatial resolution tests of the interseismic geodetic measurements for different cell sizes (Figure S4 in the auxiliary material). As expected, the spatial resolution is higher in the regions where the density of observations is important. In northern Chile, the resolution remains high even for cells of relatively small size (60 km × 40 km) but becomes poor at distances less than 50 km from the trench axis. In Peru, the resolution starts to be high below the coastline for spatial

Table 3. Fault Geometry of the Three Rectangular Dislocations Used in This Study to Describe the Megathrust Geometry

Segment	Geographical Location	Southwestern Corner Long. (°W), Lat. (°S)	Length (km)	Depth (km)	Strike (°)	Dip (°)
1	Northern Chile	71.4, 24.2	700	70	2	18
2	Southern Peru	71.3, 19.5	700	70	311	20
3	Central Peru	76.2, 15.2	700	70	317	15

Table 4. Uniform Locked Fault Zone (LFZ) Models[a]

Model Name	LFZ Depth (km)	Rate of Moment Deficit Mo (10e + 20 Nm/a)	wrms, All Data	wrms, InSAR	wrms, GPS	wrms, GPS, North Chile	wrms, GPS, South Peru	wrms, GPS, Central Peru
LFZ10	10	1.5 ($\sim M_w$7.3)	10.5	8.0	11.2	12.8	30.8	8.7
LFZ23	23	3.2 ($\sim M_w$7.6)	8.1	6.0	8.6	9.5	23.8	7.0
LFZ30	30	4.5 ($\sim M_w$7.7)	7.5	8.1	7.3	8.0	20.1	5.9
LFZ44	44	6.5 ($\sim M_w$7.8)	5.4	3.3	5.9	7.5	16.2	3.9
LFZ50	50	8.4 ($\sim M_w$7.9)	7.0	6.7	7.2	7.3	19.7	3.5
LFZ64	64	10.0 ($\sim M_w$7.9)	8.7	10.4	8.2	7.7	22.5	4.6
LFZ70	70	11.6 ($\sim M_w$8.0)	9.3	11.0	8.7	8.1	24.0	5.4

[a]Column 2 lists the depth of the downdip limit of the LFZ. Column 3 is the annual rate of moment deficit computed with an average convergence rate of 63 mm/a and the Earth structure described in Table 2. Columns 4, 5 and 6 are the weighted root mean square of the residuals (wrms, in mm/a) respectively for the whole geodetic measurements, only the InSAR data and only the GPS data. Columns 7, 8 and 9 report the wrms computed for regional subset of GPS data corresponding to northern Chile, southern and central Peru.

cells size of 120 km × 60 km but remains poor close to the trench even for larger cells size. The resolution is generally poor close to the trench especially in northern Chile and southern Peru but is relatively high when the coastline (and hence the location of the measurement) is closer to the trench as it is the case in the region where the Nazca ridge subducts.

[19] In the following, we test first a 2-plate model by assuming that the pattern of interseismic deformation depends only on the spatial distribution of coupling on the megathrust. Then, we explore 3-plate models that allow shortening in the sub-Andes and analyze its effects on the megathrust coupling distribution.

4.3. ISC Pattern of 2-Plate Model

[20] We first invert the interseismic geodetic data with the hypothesis that all the convergence between Nazca and South America is accommodated along the megathrust. We look for the interplate interseismic coupling (ISC), a ratio defined as:

$$ISC = \frac{v_0 - v}{v_0} \quad (3)$$

where v is the slip-rate along the megathrust during the interseismic period and v_0 is the long-term slip rate imposed by plate convergence. Consequently, an ISC of 0 would indicate a total creeping ($v = v_0$) while an ISC of 1 would correspond to full locking.

[21] The interseismic coupling map issued from formal inversion of the geodetic data is presented in Figure 3 (top) (model Short 0 in Table 5). As expected spatial coupling variation improves the ability of the model to fit the data over a simple uniform LFZ model. The distribution of ISC from Lima to Antofagasta appears to be very heterogeneous and can reach locally an ISC value of 1. The areas of high ISC are located offshore Lima, in southern Peru and in northern Chile. Each of those regions of high ISC correspond to the location of great ($M_w > 8.5$) earthquakes in the past such as the 1746, 1868 and 1877 events as discussed further in the text. In the regions where the Nazca ridge and the Nazca fracture zone enter in subduction, the ISC is lower than in surrounding regions signaling that aseismic slip is much higher there. The rate of moment deficit integrated over the megathrust interface from Lima to Antofagasta equals 5.1 × 10e + 20 Nm/a (nearly equivalent to a $M_w = 7.8$ earthquake per year).

4.4. ISC Pattern of 3-Plate Models

[22] One way to further improve the fit to the geodetic data is to take into account that a fraction of the plate convergence is accommodated by back-arc shortening in the subandean thrust-belt regions. We suppose that the Central Andes sliver, delimited by the trench to the west and by the subandean thrust-belt to the east (Figure 2), has a rigid sliver motion toward the west collinear to the Nazca/South America motion as previously proposed by *Bevis et al.* [2001]. This hypothesis seems reasonable and makes sense with geological and paleomagnetic observations [*Arriagada et al.*, 2008; *Kley and Monaldi*, 1998]. In practice, we did subtract a block motion to the geodetic measurements, using the pole of rotation as defined by *Kendrick et al.* [2003] for shortening velocities ranging from 1 to 17 mm/a (Table 5). The minimum wrms for all the geodetic data is reached for a model including an average subandean shortening of 9 mm/a (model Short9 in Table 5 and at the bottom of Figure 3).

[23] We further compute the misfits of the GPS data corresponding to northern Chile, southern Peru and central Peru in Table 5. The minimum wrms are reached for a shortening rate of about 4 mm/a in central Peru (model Short4 in Figure 4 (top)) and for a shortening rate of about 10 mm/a in northern Chile and southern Peru (model Short10 in Figure 4 (bottom)). The ISC distribution of these 3-plate models (Figure 4) indicates clearly less coupling and a distribution rougher than for the 2-plate models. As shortening is increased, the asperities (high ISC) become smaller while aseismic areas (low ISC) widen. The 3-plate models Short4 and Short10 have respectively rates of moment deficit (integrated over the whole study area) of 4.3 × 10e + 20 Nm/a, corresponding to a $M_w = 7.6$ earthquake per year, and 3.0 × 10e + 20 Nm/a, corresponding to a $M_w = 7.5$ earthquake per year. The rate of moment deficit of the 2-plate model Short0 is reduced by about 15% for 3-plate model Short4 and by about 40% for model Short10. This indicates that the amount of back-arc shortening has a significant impact on the distribution of ISC, and needs to be properly estimated in order to assess the amount of coupling on the megathrust and its associated rate of moment deficit.

4.5. Along-Trench Variations of the Rate of Moment Deficit

[24] By analogy with the seismic moment, the moment deficit accumulating on a fault during the interseismic phase

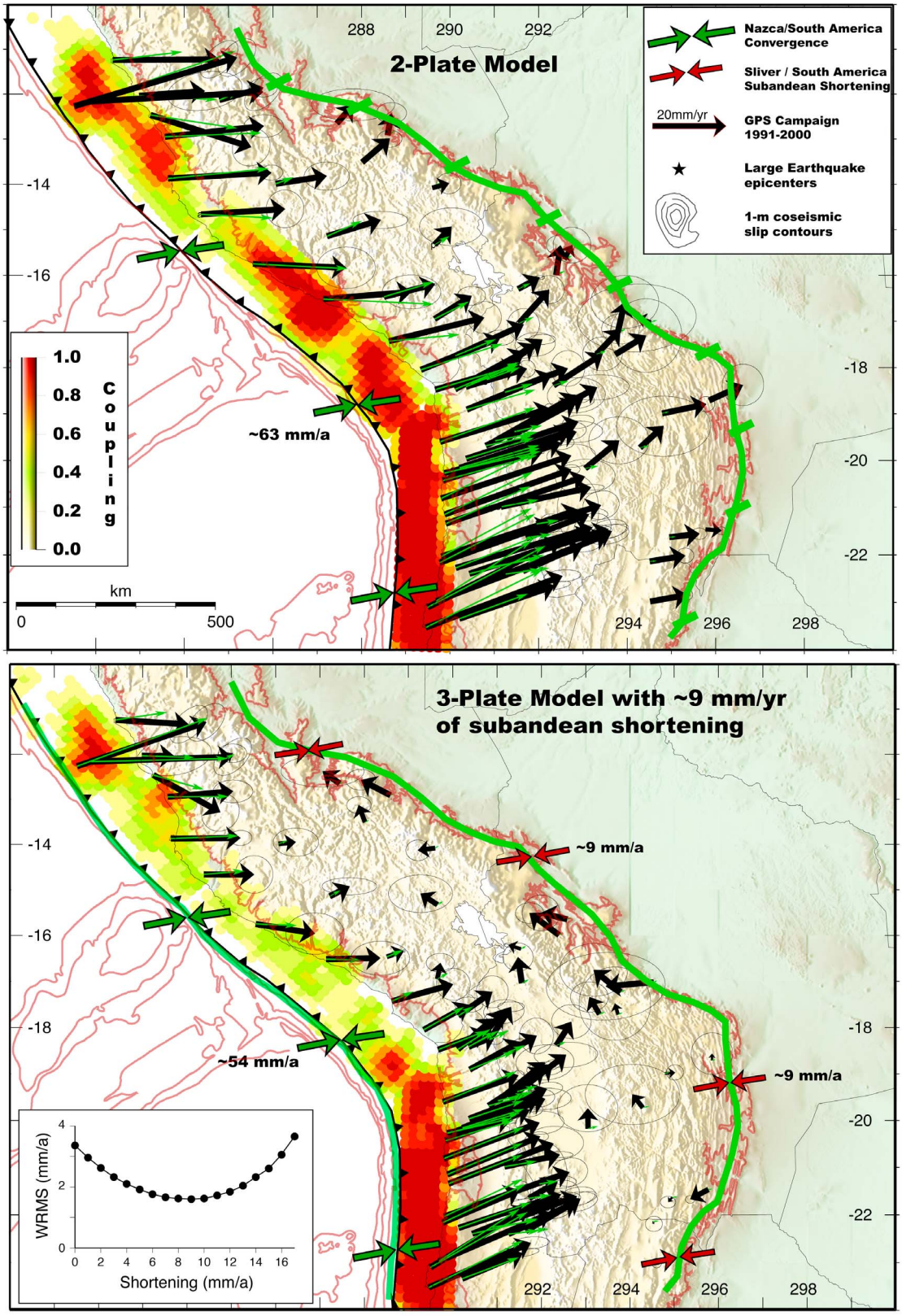
2-Plate Model
Nazca/South America Convergence
Sliver / South America Subandean Shortening
20mm/yr
GPS Campaign 1991-2000
Large Earthquake epicenters
1-m coseismic slip contours
Coupling
1.0
0.8
0.6
0.4
0.2
0.0
~63 mm/a
km
0
500
288
290
292
294
296
298
-14
-16
-18
-20
-22
3-Plate Model with ~9 mm/yr of subandean shortening
~9 mm/a
~54 mm/a
~9 mm/a
WRMS (mm/a)
Shortening (mm/a)

Figure 3

Table 5. Models Issued From Joint Inversions of All the Interseismic Geodetic Data (InSAR and GPS)[a]

Model Name	Back-Arc Shortening (mm/a)	Mo (10e + 20 Nm/a) ($\sim M_w$)	wrms, All Data	wrms, InSAR	wrms, GPS, Chile	wrms, GPS, S. Peru	wrms, GPS, C. Peru
Short0	0	5.1 ($\sim M_w$ = 7.7)	3.0	2.3	4.1	8.9	1.3
Short1	1	4.9	2.9	2.1	3.8	8.3	1.3
Short2	2	4.7	2.7	2.0	3.6	7.8	1.2
Short3	3	4.5	2.5	2.0	3.4	7.3	1.1
Short4	4	4.3 ($\sim M_w$ = 7.6)	2.4	1.9	3.2	7.0	1.0
Short5	5	4.1	2.3	1.8	3.0	6.7	1.1
Short6	6	3.9	2.2	1.7	2.9	6.4	1.2
Short7	7	3.7	2.2	1.7	2.7	6.2	1.2
Short8	8	3.5	2.1	1.6	2.7	6.3	1.3
Short9	9	3.2 ($\sim M_w$ = 7.5)	2.0	1.5	2.7	6.1	1.4
Short10	10	3.0	2.1	1.5	2.6	6.0	1.5
Short11	11	2.7	2.2	1.6	2.7	6.4	1.7
Short12	12	2.5	2.3	1.7	2.8	6.7	1.8
Short13	13	2.2	2.4	1.7	2.9	7.0	2.0
Short14	14	1.9 ($\sim M_w$ = 7.4)	2.5	1.7	3.1	7.5	2.3
Short15	15	1.8	2.7	1.8	3.2	7.9	2.5
Short16	16	1.7	2.7	1.9	3.2	8.0	2.6
Short17	17	1.5 ($\sim M_w$ = 7.3)	3.6	2.0	4.1	10.7	3.5

[a]The amount of shortening accommodated the in subandean region is listed in column 2. Model Short0 (Figure 4, top) corresponds to the 2-plate model. The minimum wrms of all the data listed in column 4 is reached for 3-plate model Short9 (Figure 4, bottom) that includes an average back-arc shortening of 9 mm/an. However, if we consider separately regional subset of GPS data corresponding to northern Chile, southern Peru or central Peru (columns 6 to 8), the minimum wrms is reached for different model. Whereas model Short4 explains best the GPS data in central Peru (Figure 5, top), model Short10 fits best the GPS data in northern Chile and southern Peru (Figure 5, bottom). The rate of moment deficit associated with the 3-plate models Short4 and short10 is respectively reduced by about 20 to 40% compared to the rate of moment deficit of the 2-plate model Short0.

can be estimated assuming a back slip dislocation and double-force couple. The LFZ embedded in an elastic medium is mathematically modeled by a back slip offset rate $d(v_0\text{-}v)(t)/dt$ across a surface S whose moment is:

$$\frac{dMo(t)}{dt} = \mu S \frac{d(vo - v)(t)}{dt} \tag{4}$$

where $dMo(t)/dt$ is the rate of moment deficit, $d(vo\text{-}v)(t)/dt$ the mean convergence rate on the interface and μ the average rigidity of the medium. Introducing the recurrence time T between large earthquakes, the moment deficit ΔMo of a steady state interseismic process may be written as:

$$\Delta Mo = \int_{o \le t' \le T} \left(\frac{dMo(t')}{dt} \right) dt' \tag{5}$$

We can use the definitions above to compute the along-strike distributions of the rate of moment deficit for all models listed in Table 5. For each model we computed the moment deficit tensors at each cell. Then at a given location along the trench, we sum up the moment deficit of each cell in the downdip direction. This summation will provide the along-strike distributions of the rate of moment deficit shown in Figures 5 (right) and 6 (right) where the maximum distribution corresponds to model Short0 and the minimum distribution to model Short17 (Table 5).

[25] Figure 5 shows the best fitting 3-plate ISC map for Peru (model Short4) together with the along-strike variations of the rate of moment deficit. The pattern of coupling is very heterogeneous, and shows four highly coupled patches, each with a dimension greater than 100 km. The most prominent aseismic creeping patches (low ISC area of about 0.4) stand in the regions where the Nazca ridge and the Nazca fracture zone are subducting. Figure 6 reports the best fitting 3-plate ISC map for northern Chile (model Short10) together with the corresponding along-strike variations of the moment deficit rate. ISC appears to be very high from the Mejillones Peninsula to about 100 km south of Arica. No significant aseismic patch (area of low ISC) is highlighted but we can observe some slight variations around Iquique possibly

Figure 3. Distribution of interseismic coupling on the Peru-Chile megathrust derived from the inversion of the geodetic data compiled in this study. (top) The 2-plate model that ignores subandean shortening (model Short0 in Table 5). The coupling map shows four highly coupled patches: one about 500 km-long in north Chile, two of about 200–300 km in southern Peru and one of about 400 km in central Peru offshore Lima. Aseismic slip occurs in the areas where the ISC is low like in the region where the Nazca ridge subducts. Observed and predicted horizontal GPS displacements appear respectively as black and green vectors. The rate of accumulation of moment deficit integrated over the whole Central Andes megathrust is estimated to 5.1×10^{20} Nm/a. (bottom) The 3-plate model that accounts for 9 mm/a of subandean shortening (model Short9 in Table 5). Inset shows how the weighted root mean square of the residuals varies as function of the assumed subandean shortening rate (Table 5). Note that the GPS velocities plotted here are corrected for the assumed rigid block motion collinear to the Nazca/South America convergence direction for an average rate of 9 mm/a. The rate of accumulated moment deficit of the 3-plate model Short9 is reduced by 37% compared to the 2-plate model.

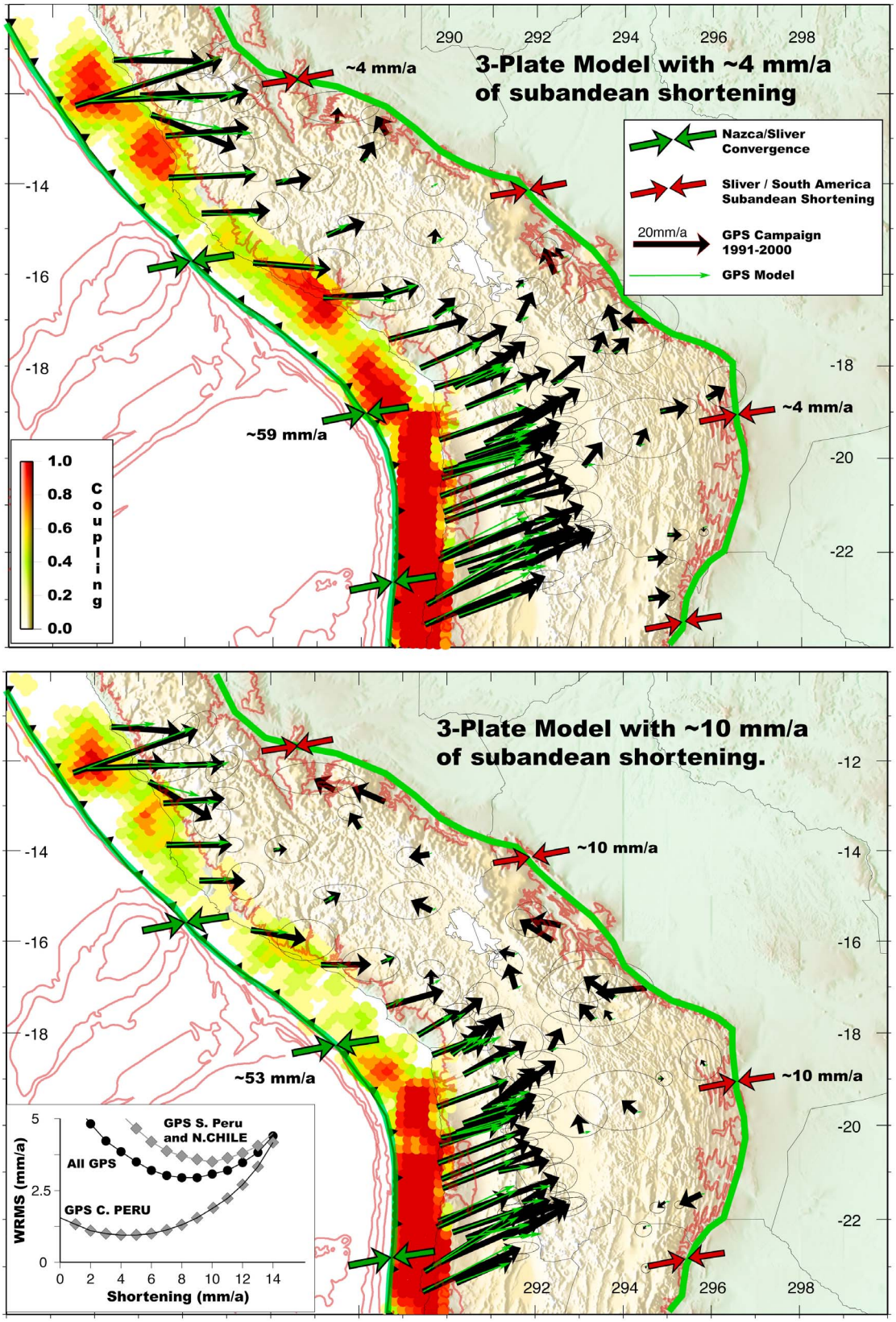
3-Plate Model with ~4 mm/a
of subandean shortening
~4 mm/a
~59 mm/a
~4 mm/a
Nazca/Sliver
Convergence
Sliver / South America
Subandean Shortening
20mm/a
GPS Campaign
1991-2000
GPS Model
Coupling
1.0
0.8
0.6
0.4
0.2
0.0
290
292
294
296
298
-14
-16
-18
-20
-22
3-Plate Model with ~10 mm/a
of subandean shortening.
~10 mm/a
~53 mm/a
~10 mm/a
-12
WRMS (mm/a)
Shortening (mm/a)
GPS S. Peru
and N.CHILE
All GPS
GPS C. PERU
0
2
4
6
8
10
12
14
2.5
5

Figure 4

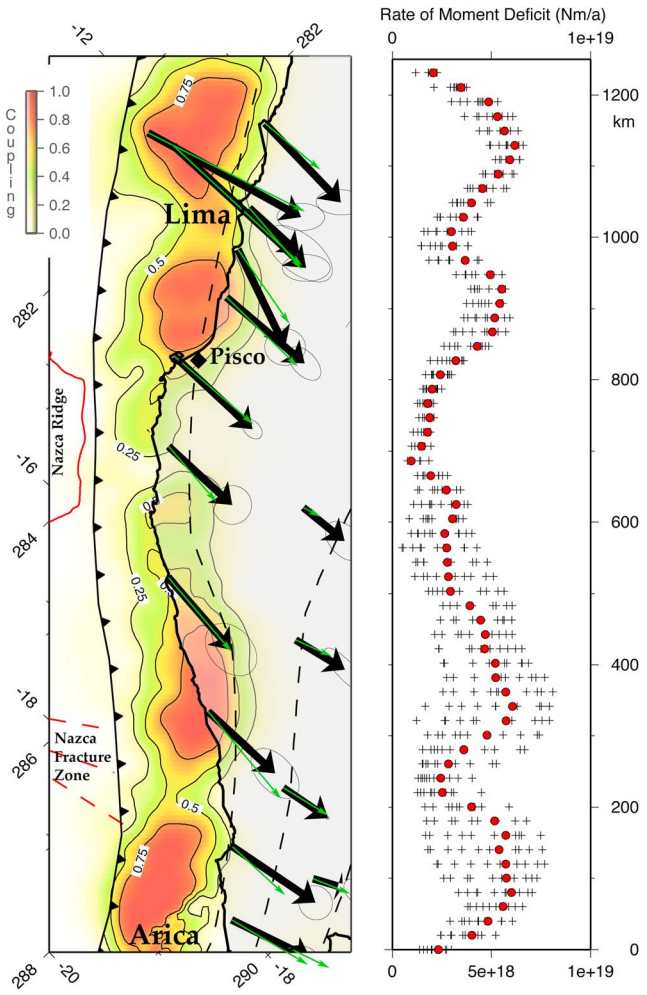

Figure 5. (left) Best interseismic coupling (ISC) model for Peru. ISC (see color scale) varies between 0 and 1. Observed and predicted interseismic GPS displacements are shown as black and green vectors respectively. The Nazca ridge and fracture zone are shown for reference. Dashed lines show the 50-km and 100-km depth contour lines of the megathrust. (right) Along-trench variations of the rate of accumulation of moment deficit for all models listed in Table 5. Each cross represents the summation in the downdip direction of the rate of moment deficit computed at each node. The circles are for model Short4.

related to the transition between asperities, with the southern asperity about twice larger than the northern one.

[26] In order to compare our ISC maps with the recent earthquakes in the area in a consistent way, we have inverted for the slip distribution of the 1996 Nazca, 2001 Arequipa and 2007 Pisco and Tocopilla earthquakes.

5. Seismic Sources Inversion for the Megathrust Earthquakes of Nazca 1996, Arequipa 2001, Pisco 2007 and Tocopilla 2007

[27] Several studies have reported sources models of the Nazca 1996, Arequipa 2001, Pisco 2007 and Tocopilla 2007 earthquakes. Some studies have relied on teleseismic data only [*Bilek and Ruff*, 2002; *Delouis et al.*, 2009; *Giovanni et al.*, 2002; *Robinson et al.*, 2006; *Spence et al.*, 1999; *Swenson and Beck*, 1999; *Tavera et al.*, 2002] while others have relied on geodetic measurements only (GPS and/or InSAR) or jointly with seismic data [*Biggs et al.*, 2009; *Béjar-Pizarro et al.*, 2010; *Motagh et al.*, 2008; *Pritchard and Fielding*, 2008; *Pritchard et al.*, 2007; *Salichon et al.*, 2003; *Sladen et al.*, 2010]. We determine new source models for these earthquakes to ensure consistency, regarding the geometry of the plate interface and the assumed Earth structure model, with our modeling of interseismic strain. Our source models are only marginally different from the models proposed by previous studies taking geodetic data into account. The seismic moment is meant to characterize the cumulative slip during the earthquake but it depends actually on frequency cut-off of the data used for its determination. Typically, body wave data give the moment with cut frequency lower than a few seconds, long-period surface-wave and free-oscillation lower than a few minutes to hours. Geodetic data are not limited by low frequency and recorded also displacements generated by aseismic slip. Then, the seismic moment estimated from seismological data (surface-wave, body wave, free-oscillations…) is always lower than the geodetic moment determined from geodetic measurements (GPS, InSAR, satellite image pixel correlation…), which often include a fraction of pre- and postseismic slip. Moreover, fault geometry and Earth structure might vary significantly from one model to another making it difficult to compare previously published models with our ISC maps. Sensitivity tests for variable dip geometry and Earth structure were carried on and are reported in the auxiliary material (Tables S1 and S3 and Figure S5). These tests emphasize the importance of using the same geometry and Earth structure when comparing models and moments.

[28] We have not removed the contribution of postseismic deformation in the geodetic data for two reasons: (i) in most cases the data available do not allow to do this easily for lack of continuous time series, (ii) our intent aim is to compare the moment released during seismic transient slip events (using the earthquake slip models derived below) with the accumulated moment deficit since the last major earthquake (obtained considering the ISC maps). In this

Figure 4. Best geodetic-fitting interseismic coupling distributions for Peru (at the top of the map) and for Chile (at the bottom of the map). The GPS velocities were corrected assuming a Central Andean block motion with (top) 4 mm/a and (bottom) 10 mm/a. Figure 4 (top) shows the 3-plate model for 4 mm/a of shortening (model Short4 in Table 5). Figure 4 (bottom) shows the 3-plate model Short10 for 10 mm/a of shortening (model Short10). Inset shows the variations of the wrms of the residuals of the GPS data as function of the subandean shortening. It shows that whereas the geodetic data located in central Peru (north of 17°S) are best fitted with 3-plate models including ~4 mm/a of subandean shortening, the geodetic data in southern Peru and northern Chile (south of 17°S) are better fitted with 3-plate models including 10 mm/a of shortening. The rates of moment deficit associated with 3-plate models Short4 and short10 are respectively reduced by about 15% and 40% compare to the 2-plate model (shown in Figure 3 (top)).

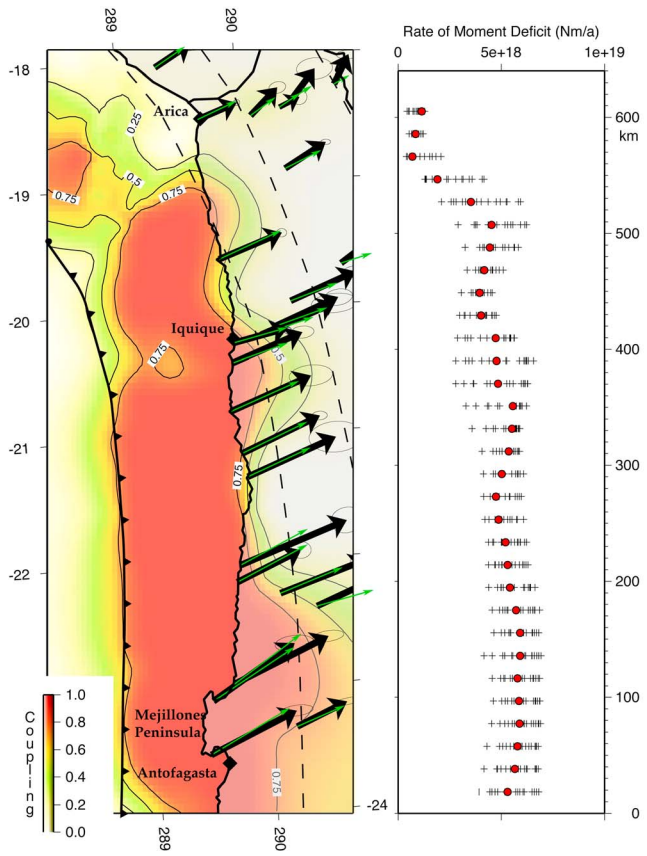

Figure 6. (left) Best interseismic coupling model for Chile. Observed and predicted interseismic GPS displacements are reported as black and green vectors respectively. (right) Along-trench variation of the rate of accumulation of moment deficit for all models listed in Table 5. Each cross represents the summation in the downdip direction of the rate of moment deficit computed at each node. The red circles are for model Short10.

perspective, it is actually more appropriate to include the moment released by seismic slip and afterslip as they jointly contribute to release interseismic elastic strain. In theory we should consider the total moment released until afterslip rate decreases below the long-term slip rate (to be consistent with our definition of transient slip events). In practice due to the typical values of the relaxation times and the 1/t decay of afterslip, >75% of the total postseismic moment released in the long term is generally released in the first three months that follow such large earthquakes. Doing so, we also determine ruptured areas which are somewhat larger that the strictly seismogenic area due to diffusion of afterslip in the rate-strengthening areas [*Hetland et al.*, 2010; *Perfettini and Avouac*, 2007]. Most of the data we have considered embrace a few months of postseismic slip, and the geodetic moments are actually found to be systematically larger than the seismic moments (Table 1).

[29] Slip inversion of the co- and postseismic geodetic measurements were done using the same algorithm as described above [*Ji et al.*, 2002]. We kept the same smoothing factor than the one used for the derivation of the ISC maps (i.e., $\lambda = 0.5$). For each slip inversion we imposed the rake not to deviate more than ±20° from that reported by the CMT solution (Table 1). In each cell, slip is allowed to vary from 0 to 10 m with steps of 0.5 m. The moment is not constrained in these inversions. Sensitivity tests of the dip of the megathrust (between 5° to 30°) were performed separately for each earthquake (see Table S4 and Figure S6 in the auxiliary material). The optimal dip angles (in terms of minimum wrms of the residuals) fall in the range of the assumed geometry and are also consistent with the dip angles of the 1st nodal plane of the Harvard CMT (listed in column 7 of Table 1), especially for the Arequipa and Tocopilla earthquakes. We found that the seismic geodetic data are best fitted for the M_w = 7.7 Tocopilla earthquake assuming a 18°-dipping slab interface, the M_w = 8.4 Arequipa and the M_w = 7.7 Nazca earthquakes assuming a 20°-dipping slab, and the M_w = 8.0 Pisco earthquake assuming a 15°-dipping slab. These optimal dip angles are the same as for the interseismic model, and therefore the comparison between ISC and coseismic slip is truly done using the same geometry.

[30] Observed and predicted geodetic (InSAR and GPS) displacements associated with each earthquake are reported in Figure 7. The slip distributions determined from our nonlinear inversions are shown in Figure 1 and together with the inverted rake on each node in Figure S7 in the auxiliary material. For each earthquake, the inverted rake direction is consistent with the average slip direction of the focal mechanisms. It is also consistent with the direction of plate convergence, suggesting that there is very little or no slip partitioning. The modeled geodetic focal mechanism is in good agreement with the Harvard CMT solution. The geodetic moment associated with the Arequipa earthquake is found to be 5.2e + 10^{21} Nm ($M_w \approx 8.4$), 1.5e + 10^{21} Nm ($M_w \approx 8.1$) for the Pisco earthquake, 0.53e + 10^{21} Nm ($M_w \approx 7.8$) for the Nazca earthquake, and 0.67e + 10^{21} Nm ($M_w \approx 7.9$) for the Tocopilla earthquake (Table 1). For the Arequipa earthquake, the cumulative seismic moment of the M_w = 8.4 main shock and its M_w = 7.61 aftershock equals 4.99e + 10^{21} Nm, which is relatively close to the geodetic moment of 5.2e + 10^{21} Nm resulting from our inversion. The geodetic moments associated with the Nazca, Pisco and Tocopilla earthquakes are found to be respectively 17%, 35% and 42% higher than the seismic moments reported in the CMT catalog (Table 1), a difference attributed to the postseismic deformation included in the measurements as discussed above.

6. Seismic Potential of the Central Andes Megathrust

[31] Figure 8 shows the along-trench variations of the seismic moment released by historical and recent large megathrust earthquakes offshore Peru. Each curve is constructed from the summation of the seismic moment tensors at all nodes in the slip model within 20-km trench-normal slices. The distribution of moment released by historical events is estimated using the ruptures extent and magnitude as proposed by *Dorbath et al.* [1990]. The cumulative seismic moment released by the M_w~8.0 megathrust earthquakes sequence of 1942, 1966, 1974 and 2007 ranges between 26 and 52% of the moment that was released during the great 1746 M_w~8.6–8.8 earthquake. It appears also that the 1996

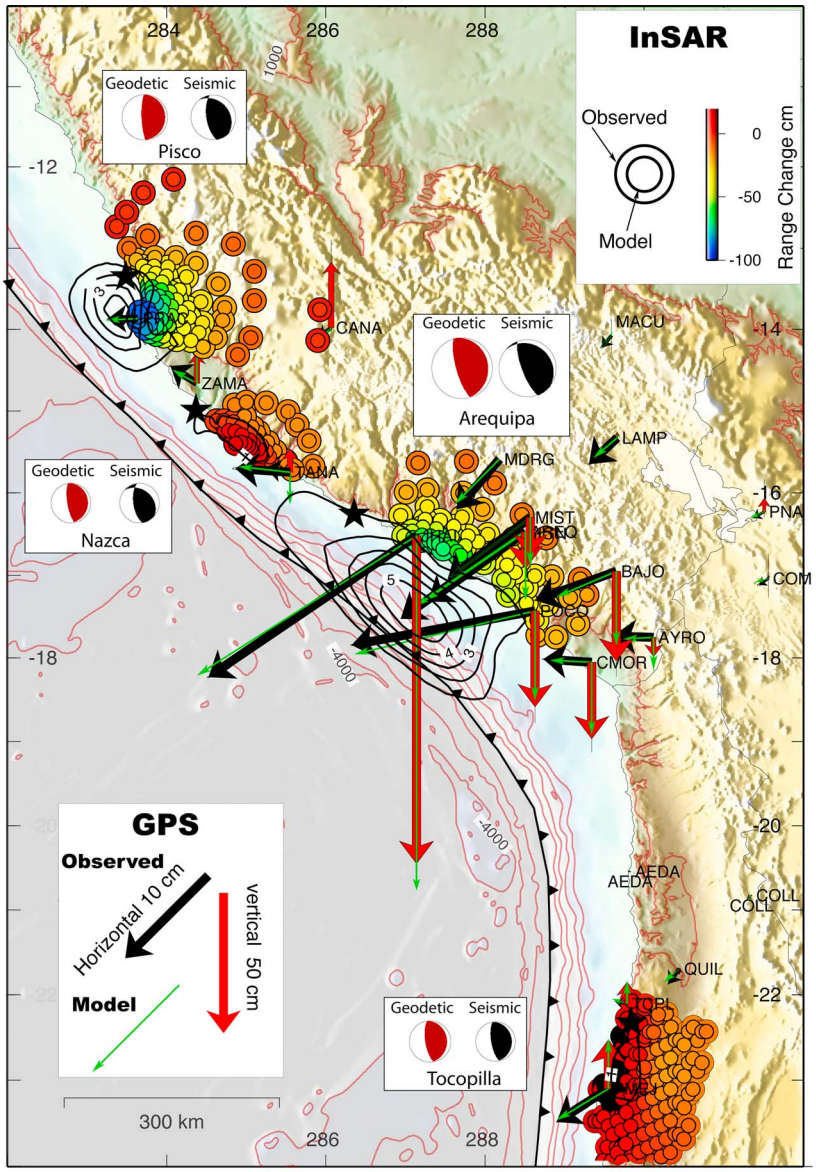

Figure 7. Coseismic geodetic displacements associated with the 2007 Pisco, 1996 Nazca, 2001 Arequipa and 2007 Tocopilla earthquakes. Slip distribution contours are reported each 1-m. Detail slip distributions with the inverted rake on each cell are reported in Figure S7 in the auxiliary material. Observed horizontal and vertical GPS measurements appear as black and red vectors respectively. The predicted GPS displacements are in green. Observed and predicted InSAR measurements are respectively large and small circles with the associated color table indicating the range change in line of sight of the ERS and Envisat satellites. The geodetic focal mechanisms (red beach ball) determined from our seismic source inversions are quite consistent with the focal mechanisms from the Harvard catalog (black beach ball).

Nazca earthquake released about 25% of the moment released during the 1942 M_w∼8.2 earthquake. A similar comparison indicates that the 2001 Arequipa events (M_w = 8.4 and its M_w = 7.6 aftershock) seem to have released less than 50% of the moment that was released during the great 1868 M_w∼8.8 earthquake.

[32] The slip sources of the M_w = 8.0 Pisco, M_w = 7.7 Nazca and M_w = 8.4 Arequipa earthquakes are compared with the ISC map determined for the 3-plate model Short4 in central Peru and model Short10 in southern Peru (Figure 9). All these seismic sources coincide with patches highly (for Pisco and Arequipa) or partially (for Nazca) locked before the earthquakes. Because of the particularly low resolution on interseismic coupling close to the trench it makes more sense to compare along strike variation of coupling and seismic moment released than along dip variations. All the recent large ruptures appear to have stopped in areas where the ISC is low suggesting that aseismic patches may play the role of a barrier to seismic rupture propagation. In the region where the Nazca ridge subducts, the ISC appears to be as low as 0.4 meaning that about 60% of slip there is aseismic. In the last 500 years, no great earthquake with moment

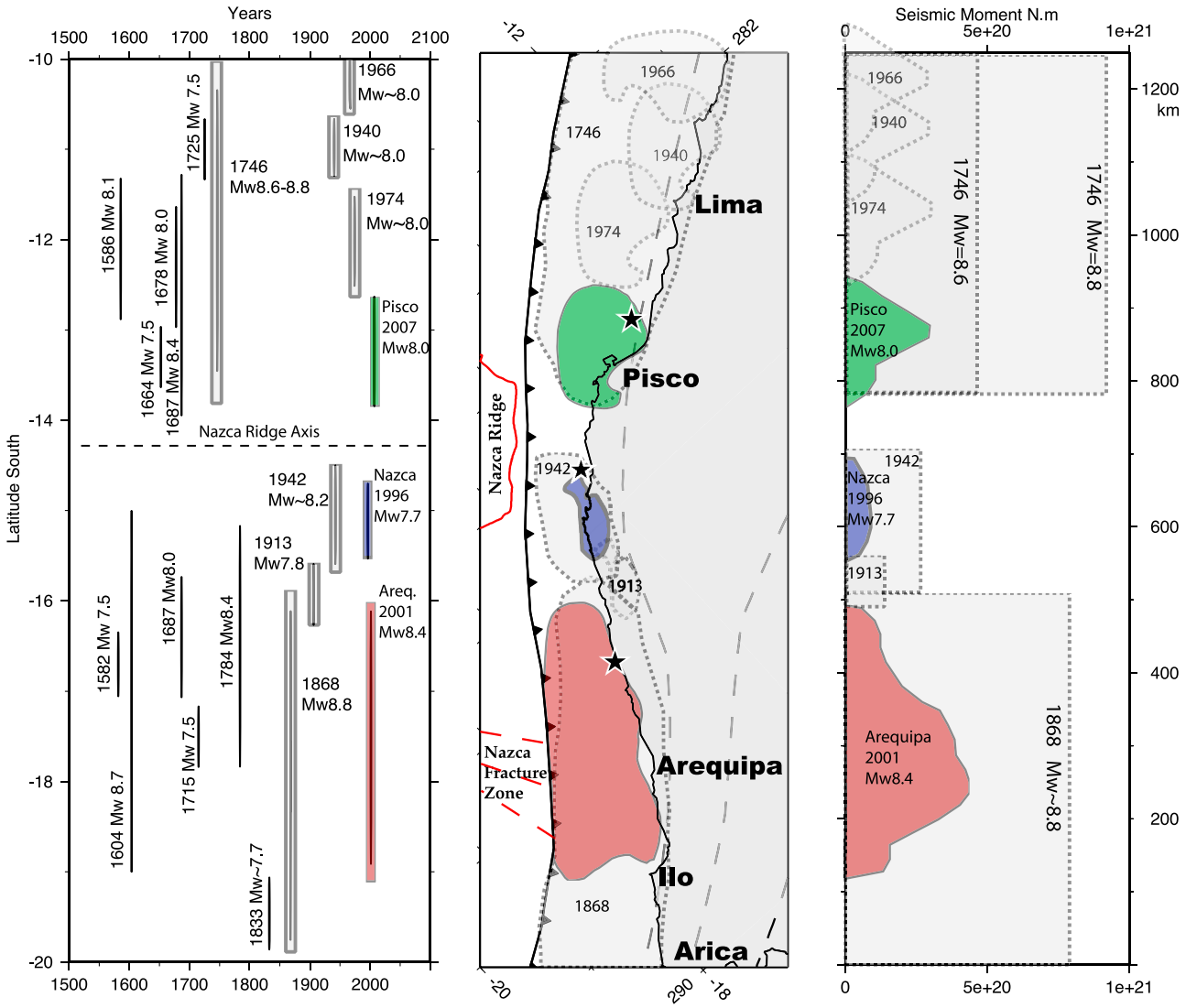

Figure 8. Historical and recent large megathrust earthquakes in central and southern Peru. (left) Dates, extents and magnitudes of historical megathrust earthquakes. (middle) We used these parameters and the ruptures areas to estimate the distribution of moment released by historical events of 1746 (M_w8.6–8.8), 1868 (M_w8.8), 1940 (M_w8.0), 1942 (M_w8.2), 1966 (M_w8.0), 1974 (M_w8.0) and 1913 (M_w7.8). To improve consistency the rupture areas of the M_w~8.0 1940/1996/1974 earthquakes (shown in Figure 1), were rescaled using the rupture area of the 2007 M_w~8.0 Pisco earthquake as a reference. (right) The along-trench variations of the seismic moment associated to each earthquake.

magnitude $M_w > 8.5$, is known to have ruptured through this ridge. North of the Nazca ridge, if we assume the actual rate of moment deficit to have been stationary, the moment deficit accumulated since 1746 indicates that a similar great event is over-due. Indeed, the cumulative moment released by the sequence 1940–2007 represents only 23% of the moment deficit accumulated since 1746 suggesting that a significant amount of seismic moment is still to be released on that 500-km long segment. South of the Nazca ridge, the moment deficit since 1942 has accumulated enough moment to produce a same magnitude event. Finally, the moment deficit accumulated since 1868 was partially released during the 2001 $M_w = 8.4$ Arequipa earthquake but we can observe that the potential of that segment is still high since the southern portion of the 1868 rupture has not broken yet.

[33] In Chile, the slip distribution of the $M_w = 7.7$ Tocopilla earthquake is reported on the coupling map of the 3-plate model Short10 (Figure 10). The rupture of this earthquake occurred in an area of the megathrust that was highly locked before the earthquake. However, this rupture is limited to a small fraction in the downdip end of the LFZ and most of the northern Chile seismic gap remains still to break. The seismic moment released by the 2007 Tocopilla earthquake represents only 3 to 7% of the moment released during the great 1877 earthquake whether it was a magnitude $M_w = 8.5$ or a $M_w = 8.8$ event. Model Short10 indicates that the Northern Chile seismic gap may have accumulated enough moment deficit since 1877 to produce an earthquake with $M_w > 8.5$.

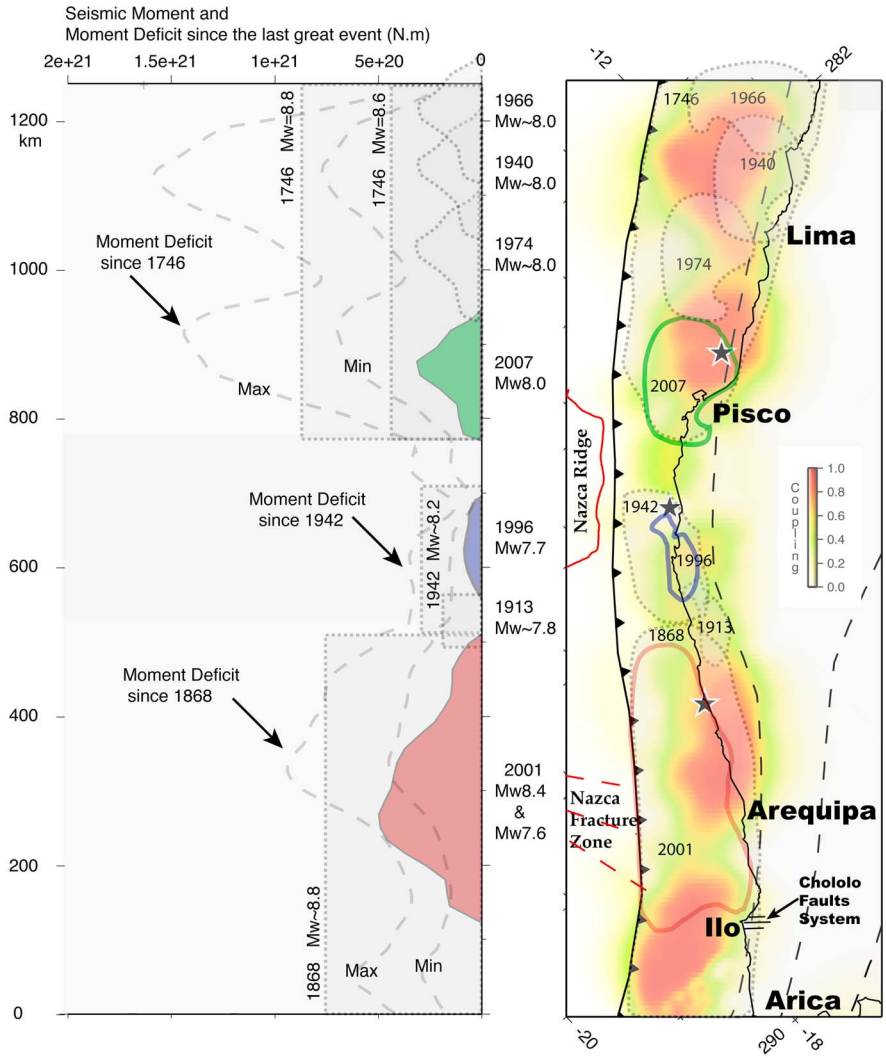

Figure 9. Comparison of interseismic coupling along the megathrust with ruptures of large megathrust earthquakes in central and southern Peru. (left) Interseismic coupling map for 3-plate model Short4; it indicates that where the Nazca ridge and the Nazca fracture zone subduct, the interseismic coupling is low. The largest earthquake there is the M_w8.1–8.2 earthquake of 1942. It is not clear whether the 1942 rupture propagated through the Nazca ridge or stopped south of it. High interseismic coupling patches correlate well with regions that experienced great megathrust earthquake M_w8.8 in 1868 and M_w8.6–8.8 in 1746. In the south, the presence of two wide asperities separated by a wide aseismic patch may explain partially the seismic behavior of this segment in the last centuries. Individual ruptures of these asperities would produce M_w~8 events, as in 2001, but their simultaneous rupture could generate great $M_w > 8.5$ earthquakes as in 1604 or 1868. The along-strike coincidence of the high coupling areas (orange-red) with the region of high coseismic slip during the 2001 Arequipa and 2007 Pisco earthquakes suggests that strongly coupled patches during the interseismic period may indicate the location of future seismic asperities. (right) Moment deficit (dashed lines) since the last great earthquake of 1868, 1942 and 1746 compared with the seismic moment released during recent and historical earthquakes of Figure 8. The moment deficit is computed from the rate of moment deficit predicted by model Short4 considering a steady state interseismic process (Max) or 50% of it (Min) to account for time-variable interseismic process and transient events.

6.1. The 1746 Pisco-Lima-Huacho Segment

[34] The rate of moment deficit of model Short4 over the 1746 rupture segment is 0.83 × 10e + 20 Nm/a. In the last 264 years, it leads to a moment deficit of about 22 × 10e + 21 Nm considering a steady state interseismic process. This corresponds to 45–90% of the moment released during the great 1746 M_w8.6–8.8 earthquake. The cumulative seismic moment released by the M_w~8.0 megathrust earthquakes sequence of 1940, 1966, 1974 and 2007 is about 5 × 10e + 21 Nm. This leaves for the segment Pisco-Lima-Huacho a seismic potential of about 17 × 10e + 21 Nm which corresponds to an earthquake of moment magnitude M_w~8.7. If

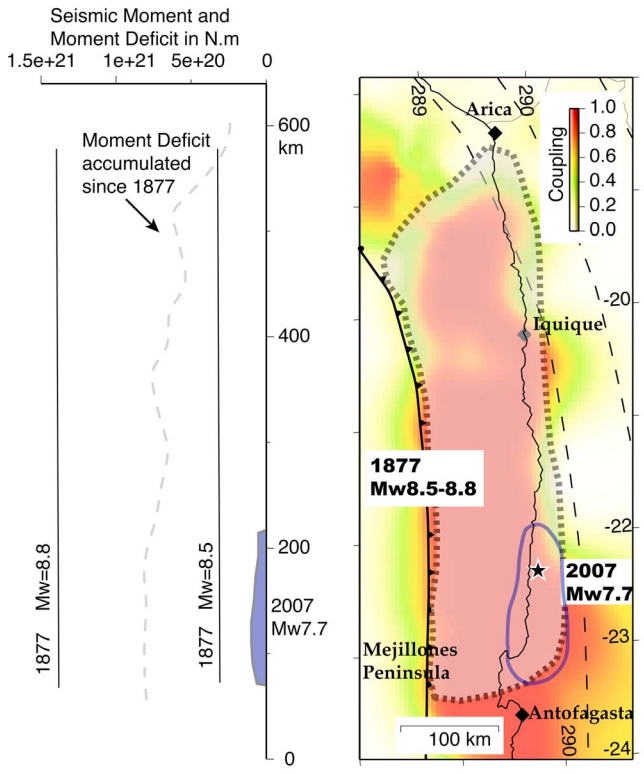

Figure 10. Comparison of interseismic coupling along the megathrust with ruptures of large megathrust earthquakes in north Chile. (right) Interseismic coupling pattern determined for the 3-plate model Short10 indicates a very high coupling over most of that area decreasing slightly offshore Iquique and more significantly offshore Arica. The 1-m slip contour of the Tocopilla earthquake of 2007 (blue line) appears to have ruptured only a small portion of the southern downdip end of the locked fault zone and of the 1877 event. (left) The moment deficit accumulated since 1877 computed from model Short10, assuming the ISC has not varied with time, and the seismic moment released by the 1877 (M_w8.5–8.8) and 2007 (M_w = 7.7) earthquakes. The seismic moment released by the 2007 event represents 4% of the moment deficit accumulated since 1877.

we accept that a maximum of 50% of this moment could have been released by non steady state interseismic process and slow slip events, this potential is reduced to a moment magnitude equivalent to a M_w∼8.5 event.

6.2. The 1942 Nazca Segment

[35] Above the Nazca ridge, the proportion of aseismic slip appears to be more important (60%) than in the adjacent segments. The recent 1996 Nazca M_w = 7.7 and 2007 Pisco M_w = 8.0 earthquakes have stopped respectively just south and north of the Nazca ridge. The rate of moment deficit of the Nazca segment extending from 14°S to 16°S is 0.4 10e + 20 Nm/a. At that rate, the cumulative moment deficit since 1942 would be 2.9 × 10e + 21 Nm and only 0.5 × 10e + 21 Nm was released during the 1996 event. This leaves a seismic potential of 2.4 × 10e + 21 Nm equivalent to a M_w∼8.2 earthquake there. A minimum of M_w∼8.0 earthquake is proposed in case of a nonsteady state interseismic process.

6.3. The 1868 Arequipa Segment

[36] The rate of moment deficit over the 1868 rupture segment is about 0.85 × 10e + 20 Nm/a. The moment deficit accumulated at the current rate since 1868 reaches 12 × 10e + 21 Nm. This is equivalent to 67% of the moment released during the great 1868 M_w∼8.8 earthquake. The seismic moment released by the Arequipa earthquake being 5.2 × 10e + 21 Nm, this leaves a seismic potential of 6.8 × 10e + 21 Nm (M_w∼8.5) over the whole 1868 rupture. The southern asperity that did not break in 2001 have accumulated alone a seismic moment of 4.8 × 10e + 21 Nm equivalent to a M_w∼8.4 earthquake. Considering a nonsteady state interseismic process, this would lead to a minimum seismic potential equivalent of M_w∼8.3 earthquake for the whole 1868 rupture segment and M_w∼8.1 for the southern Peru asperity alone.

6.4. The 1877 North Chile Segment

[37] In Northern Chile, the rate of moment deficit over the 1877 rupture segment is about 1.3 × 10e + 20 Nm/a. It corresponds to a cumulative moment deficit of about 17.2 × 10e + 21 Nm in 133 years. The seismic moment released by the Tocopilla earthquake represents only 4% of this moment deficit. The seismic potential left is 16.5 × 10e + 21 Nm which equals an earthquake of moment magnitude M_w∼8.8 over the whole 1877 rupture area. A minimum of M_w∼8.6 earthquake is estimated when we account for potential nonsteady state interseismic process.

7. Discussion

[38] Interseismic GPS velocities in the Central Andes have been previously interpreted based on simpler models which were considering uniform locking of the megathrust in the interseismic period down to a depth of 40–55 km and considering a mobile sliver extending from the trench to the subandean Eastern foothills [*Bevis et al.*, 2001; *Chlieh et al.*, 2004; *Gagnon et al.*, 2005]. These models were explaining the first order pattern of interseismic strain but, as observed along other subduction zones, significant lateral variations of interseismic coupling are needed to fully explain the available geodetic data set of the Central Andes. In this study, we observed that the heterogeneous pattern of interseismic coupling is consistent with the spatial distribution of recent large subduction earthquakes; the largest earthquakes ($M_w \geq 8$) all fall in areas of high ISC (Figures 9 and 10). In addition the patches of significant afterslip following the Pisco earthquake correspond to areas of low ISC, and the time-evolution of afterslip is well described by a rate strengthening friction law [*Perfettini et al.*, 2010]. This supports the idea that areas of low ISC correspond to areas where a large proportion of the megathrust is governed by a velocity strengthening friction law, while areas of high ISC are dominantly velocity weakening. Our ISC maps assume mostly aseismic creep at shallow depth near the trench. The resolution of this feature is low here because of the absence of data but it is however consistent with postseismic observations which show that this area tends to follow a rate-strengthening behavior. This is noticeable in the Sumatra area where the slip resolution at

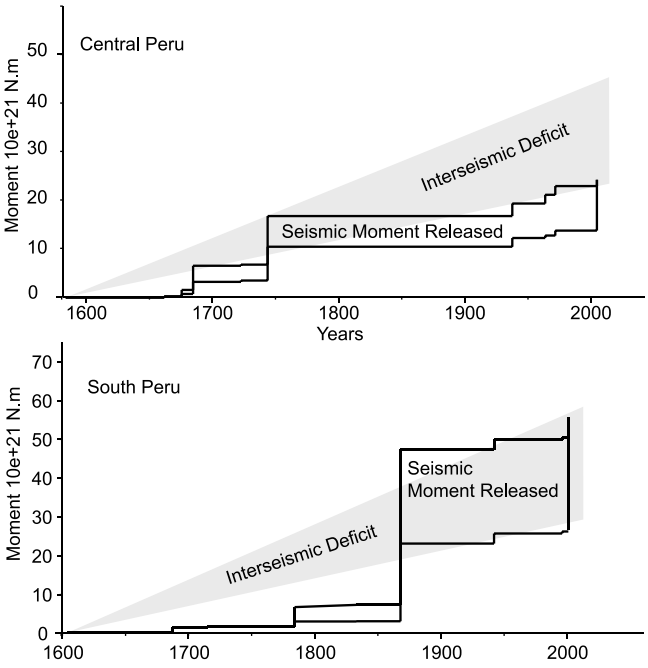

Figure 11. Cumulative deficit of moment and seismic moment released due to major subduction earthquakes since the 16th century (top) in central Peru and (bottom) in southern Peru. The cumulative deficit of moment is predicted from the rates of 3-plate models Short4 in central Peru and Short10 in southern Peru (Table 5 and Figure 4). The uncertainties of moment released by historical events lead to a minimum and maximum moment released (see Table S8 in the auxiliary material). The uncertainties on the cumulative deficit of moment allow that nonlinear interseismic and viscous processes could have released 50% of the accumulated moment deficit. The remaining fraction should reflect elastic strain available to drive future earthquakes unless it would have been totally released by anelastic deformation of the forearc.

shallow depth is better constrained due to the islands formed by the emerged outer-arc high [*Hsu et al.*, 2006]. However, the March 2011 Tohoku-Oki earthquake which released a lot of slip at shallow depth [*Simons et al.*, 2011] shows that the assumption of low interseismic coupling near the trench might be questionable. So we might actually be underestimating shallow coupling and the rate of accumulation of moment deficit in the interseismic period. Heterogeneous ISC models reveal that coupling is high only in specific areas of the megathrust embedded in aseismic creeping regions. The pattern of interseismic locking is therefore probably quite stationary reflecting the spatial distribution of the various factors that determine the friction properties of the plate interface (temperature, lithology, topography of the subducting plate or other anelastic process). Subducting heterogeneities such as fracture zones, ridges or seamounts may be an explanation for the presence of low ISC areas observed in the coupling maps.

[39] By contrast, as observed in other subduction contexts [*Kanamori and McNally*, 1982; *Konca et al.*, 2008; *Thatcher*, 1990], a given highly locked patch can generate quite different seismic sequences as the pattern of ruptures in central and southern Peru suggests (Figure 1) [*Dorbath et al.*, 1990]. The 1746 earthquake seems to have involved the simultaneous breakage of the asperities that later ruptured in 1940, 1966, 1974 and 2007. In southern Peru, the two zones of high ISC of Figure 5 failed separately during the large ($7.7 < M_w < 8.5$) earthquakes of 1784, 1833 and 2001, but seem to have ruptured simultaneously during the great ($M_w > 8.5$) earthquakes of 1604 and 1868. *Robinson et al.* [2006] have reported that a barrier has stalled the rupture of the 2001 Arequipa earthquake. This barrier is characterized by a local low slip as well as a low rupture speed. *Robinson et al.* [2006] noticed that it coincides with the Nazca Fracture Zone, a prominent feature on the subducting oceanic plate. We note that it also coincides well with an area of the slab with relatively low ISC (Figures 4 and 5). This barrier could be due to a purely geometric effect, or due to a rate-strengthening patch similar to the barrier which affected the 2007 Pisco rupture [*Sladen et al.*, 2010]. Postseismic observations following the 2001 Arequipa earthquake should help discriminate between these two possibilities.

[40] Similarly, the rupture of the Pisco earthquake showed also a 2 peaks slip distribution, with a slow rupture velocity possibly associated with the existence of a creeping patch separating the two seismic asperities [*Sladen et al.*, 2010]. The propagation of the Pisco earthquake was stopped in the south when the rupture encountered the Nazca ridge [*Perfettini et al.*, 2010]. This observation that seismic asperities are not permanent features while barriers are probably persistent, can be explained through the concept of a megathrust paved by intertwined rate-weakening and rate strengthening patches as dynamic simulations of the seismic cycle have shown [*Kaneko et al.*, 2010]. Successive rupture sequences differ depending on whether neighboring locked patches (with rate-weakening friction) rupture together or as separate events. Barriers can sometimes arrest rupture (as in the sequence occurring in central Peru since the 2nd half of the 20th century), but sometimes cannot (such as in the 1746 earthquake). The efficiency of such a barrier to arrest rupture depends on its size and frictional properties but the effect on individual rupture is not entirely deterministic as the probability -of a particular event to break through a barrier- depends on the megathrust frictional properties as well as on the detail of the pre-stress distribution which depends partly on the previous ruptures [*Kaneko et al.*, 2010]. *Kaneko et al.* [2010] found that the probability for a large earthquake to break through the aseismic patch is correlated with the interseismic coupling averaged over this patch, and that a barrier is permanent when its ISC is lower than 0.6. Although this particular value depends on the setting of their numerical simulations, such a value is actually consistent with the value of the ISC we derive along the Nazca ridge (ISC$\sim$0.4), which is a rate-strengthening area as shown by the pattern of afterslip following the Pisco earthquake [*Perfettini et al.*, 2010], and the fact that no historical earthquake seems to have propagated through this barrier.

[41] The fact that the ISC pattern (derived considering today's measurements) correlates with the location of past large earthquakes tends to suggest that the ISC pattern is stationary and probably does not vary much over a few earthquake cycles. The seismic potential estimates along the subduction megathrust rely on the assumptions that only the

large known earthquakes have contributed to strain release. If this assumption is correct, on the long-term average, the accumulated deficit of moment due to interseismic locking should equal the moment released by the known megathrust events. Let's now consider the moment deficit that must have been accumulated along the megathrust since the 16th century in southern and central Peru and compare it with the cumulative seismic moment released over the same period (Table S8 in the auxiliary material). The cumulative deficit of moment is determined from the rate of accumulation of moment deficit found for the 3-plate models Short4 in central Peru and Short10 in southern Peru (Figure 4 and Table 5) and with the hypothesis that the interseismic loading did not vary with time. For uncertainties, we accept that 50% of the cumulative deficit of moment could have been released by anelastic deformation of the forearc. Figure 11 shows that in southern Peru, the cumulative deficit of moment equals -within uncertainties- with the cumulative moment released by past large earthquakes. By contrast, the cumulative moment deficit is on average about twice higher in central Peru suggesting that there would be enough elastic strain stored in that area to drive a large megathrust event in the near future. However, we cannot totally exclude that transient slow slip events and non-uniform interseismic strain due to long-term viscous effects could have released a significant amounts of the cumulative deficit of moment. Testing this is not possible with the available information.

8. Conclusion and Perspectives

[42] The interseismic coupling pattern determined in this study shows that areas with large coupling are confined to the 0–50 km depth range, which is also the interplate seismogenic depth range. ISC drops at greater depth where aseismic slip at the plate convergence rate is inferred. This downdip transition could reflect the effect of temperature on the rate-dependency of friction or a lithological transition at the forearc Moho [*Hyndman et al.*, 1997; *Oleskevich et al.*, 1999]. If they were the only factors, frictional properties would vary along dip only, and so should interseismic locking. The lateral variations seen in the interseismic models indicate that there must be other factors (i.e., lithology, fluids, …) at play, resulting in intertwined patches with rate-strengthening and rate-weakening properties. The determination of that pattern yields insight about the potential characteristics of future large megathrust earthquakes in that area. The regions of high ISC are expected to coincide with large seismic slip. The range of possible earthquake magnitudes associated with the breaking of these locked fault zones is difficult to assess a priori from a purely kinematic analysis as neighboring locked patches may break individually or simultaneously as the historical records of past earthquakes suggest. This depends essentially on the potential of the areas with low coupling to act as a barrier to the seismic rupture propagation. This behavior is not systematic as shown from dynamic simulation studies [*Kaneko et al.*, 2010]. Some barriers, large enough or strongly rate-strengthening, may systematically arrest seismic ruptures as it seems to be the case for the region where the Nazca ridge subducts. By contrast, zones with a more subtle signature as the zone of low ISC detected in southern Peru may occasionally inhibited rupture propagation as happened in 2001, or permit thoroughgoing ruptures as happened in 1604 and 1868.

[43] The along-trench correlation between the location of large subduction earthquakes and areas of high ISC may be used to assess the size and magnitude of future large megathrust earthquakes. By estimating the interseismic moment deficit and coseismic moment released by past megathrust earthquakes, we have been able to estimate the seismic potential of 4 segments: the 1746 Pisco-Lima-Huacho segment could generate an earthquake of moment magnitude M_w∼8.5 to 8.7, the 1942 Nazca segment, a M_w∼8.0–8.2, the 1868 Arequipa segment, a M_w∼8.1–8.5 and the 1877 northern Chile gap, an earthquake of M_w∼8.6 to 8.8.

[44] These estimates are based on the hypothesis that interseismic strain of the upper crust is only elastic and doesn't vary over the seismic cycle. These two assumptions, although probably valid to first order, will need to be investigated more deeply in the future. The spatial density of geodetic measurement needs to be increased to improve the spatial resolution of the distribution of interseismic coupling. It would allow imaging better the aseismic barriers that determine partly megathrust segmentation. It would be important to determine if interseismic strain is time invariant and also to evaluate the possible contribution of aseismic transients to release strain. This calls for more effort to deploy and maintain permanent networks of geodetic stations. Finally sea-bottom geodesy [*Gagnon et al.*, 2005] would help assess better interseismic strain accumulation at shallow depth (<15–20 km) near the trench where onshore geodetic measurements provide very little resolution. This is of major importance with regard to tsunami hazard, as the frequency and magnitude of tsunamigenic earthquakes presumably depend strongly on this factor.

[45] **Acknowledgments.** The Institut de Recherche pour le Développement (IRD) of France supported the main funding for this research. Logistical support was provided by the Centre National d'Etudes Spatiales (CNES) through the Tosca grant, convention CNES/95532. The European Space Agency (ESA) provided the Envisat and ERS satellite images through CAT-1 project ID5487. We deeply thank J.P. Loveless, K. Wang and three anonymous reviewers for their constructive comments. M.C. deeply thanks Khadija and Souad Zakari for their supports. We used the Generic Mapping Tool (http://gmt.soest.hawaii.edu/) for Figures 1–11.

References

Aktug, B., et al. (2009), Deformation of western Turkey from a combination of permanent and campaign GPS data: Limits to block-like behavior, *J. Geophys. Res.*, *114*, B10404, doi:10.1029/2008JB006000.

Altamimi, Z., P. Sillard, and C. Boucher (2002), ITRF2000: A new release of the International Terrestrial Reference frame for earth science applications, *J. Geophys. Res.*, *107*(B10), 2214, doi:10.1029/2001JB000561.

Arriagada, C., P. Roperch, C. Mpodozis, and P. R. Cobbold (2008), Paleogene building of the Bolivian Orocline: Tectonic restoration of the central Andes in 2-D map view, *Tectonics*, *27*, TC6014, doi:10.1029/2008TC002269.

Audin, L., H. Perfettini, J. Avouac, D. Farber, D. De la Cruz, and M. Chlieh (2007), The 2007 Pisco earthquake (Mw8.0), Central Peru: Preliminary field investigations and seismotectonic context, *Eos Trans. AGU*, *88*(52), Fall Meet. Suppl., Abstract T33E-02.

Audin, L., P. Lacanb, H. Tavera, and F. Bondoux (2008), Upper plate deformation and seismic barrier in front of Nazca subduction zone: The Chololo fault system and active tectonics along the coastal cordillera, southern Peru, *Tectonophysics*, *459*(1–4), 174–185, doi:10.1016/j.tecto.2007.1011.1070.

Baby, P., B. Guillier, J. Oller, and G. Montemurro (1993), Kinematic model of the Subandean zone of the Santa Cruz bend (between 16°S and 19°S, Bolivia) deduced from map balancing, *C.R. Acad. Sci. Paris*, *317*(2), 1477–1483.

Baby, P., J. P. Rochat, G. Mascle, and G. Hérail (1997), Neogene shortening contribution to crustal thickening in the back arc of the Central Andes, *Geology*, *25*(10), 883–886, doi:10.1130/0091-7613.

Barke, R., S. Lamb, and C. MacNiocaill (2007), Late Cenozoic bending of the Bolivian Andes: New paleomagnetic and kinematic constraints, *J. Geophys. Res.*, *112*, B01101, doi:10.1029/2006JB004372.

Barrientos, S. E., G. Plafker, and E. Lorca (1992), Postseismic uplift in southern Chile, *Geophys. Res. Lett.*, *19*, 701–704, doi:10.1029/92GL00210.

Bassin, C., G. Laske, and G. Masters (2000), The current limits of resolution for surface wave tomography in North America, *Eos Trans. AGU*, *81*(48), Fall Meet. Suppl., Abstract S12A-03.

Beck, S. L., and S. P. Nishenko (1990), Variations in the mode of great earthquake rupture along the central Peru subduction zone, *Geophys. Res. Lett.*, *17*, 1969–1972, doi:10.1029/GL017i011p01969.

Beck, S. L., and L. J. Ruff (1989), Great earthquakes and subduction along the Peru trench, *Phys. Earth Planet. Inter.*, *57*(3–4), 199–224, doi:10.1016/0031-9201(1089)90112-X.

Béjar-Pizarro, M., et al. (2010), Asperities and barriers on the seismogenic zone in north Chile: State-of-the-art after the 2007Mw 7.7 Tocopilla earthquake inferred by GPS and InSAR data, *Geophys. J. Int.*, *183*, 390–406, doi:10.1111/j.1365-246X.2010.04748.x.

Bevis, M., R. J. Smalley, T. Herring, J. Godoy, and F. Galban (1999), Crustal motion north and south of the Arica deflection: Comparing recent geodetic results from the central Andes, *Geochem. Geophys. Geosyst.*, *1*(12), 1005, doi:10.1029/1999GC000011.

Bevis, M., E. Kendrick, R. J. Smalley, B. Brooks, R. Allmendinger, and B. Isacks (2001), On the strength of interplate coupling and the rate of back arc convergence in the central Andes: An analysis of the interseismic velocity field, *Geochem. Geophys. Geosyst.*, *2*(11), 1067, doi:10.1029/2001GC000198.

Biggs, J., D. P. Robinson, and T. H. Dixon (2009), The 2007 Pisco, Peru, earthquake (m8.0), Seismology and geodesy, *Geophys. J. Int.*, *176*(3), 657–669, doi:10.1111/j.1365-1246X.2008.03990.x.

Bilek, S. L., and L. J. Ruff (2002), Analysis of the 23 June 2001 Mw = 8.4 Peru underthrusting earthquake and its aftershocks, *Geophys. Res. Lett.*, *29*(20), 1960, doi:10.1029/2002GL015543.

Brown, L. D., R. E. Reilinger, S. R. Holdahl, and E. I. Balazs (1977), Postseismic crustal uplift near Anchorage, Alaska, *J. Geophys. Res.*, *82*(23), 3369–3378, doi:10.1029/JB082i023p03369.

Bürgmann, R., M. G. Kogan, G. M. Steblov, G. Hilley, V. E. Levin, and E. Apel (2005), Interseismic coupling and asperity distribution along the Kamchatka subduction zone, *J. Geophys. Res.*, *110*, B07405, doi:10.1029/2005JB003648.

Chen, C. W., and H. A. Zebker (2001), Two-dimensional phase unwrapping with use of statistical models for cost functions in nonlinear optimization, *J. Opt. Soc. Am.*, *18*(2), 338–351, doi:10.1364/JOSAA.18.000338.

Chlieh, M., J. B. de Chabalier, J. C. Ruegg, R. Armijo, R. Dmowska, J. Campos, and K. L. Feigl (2004), Crustal deformation and fault slip during the seismic cycle in the North Chile subduction zone, from GPS and InSAR observations, *Geophys. J. Int.*, *158*(2), 695–711, doi:10.1111/j.1365-246X.2004.02326.x.

Chlieh, M., J. P. Avouac, K. Sieh, D. H. Natawidjaja, and J. Galetzka (2008), Heterogeneous coupling of the Sumatran megathrust constrained by geodetic and paleogeodetic measurements, *J. Geophys. Res.*, *113*, B05305, doi:10.1029/2007JB004981.

Collot, J. Y., B. Marcaillou, F. Sage, F. Michaud, W. Agudelo, P. Charvis, D. Graindorge, M. A. Gutscher, and G. Spence (2004), Are rupture zone limits of great subduction earthquakes controlled by upper plate structures? Evidence from multichannel seismic reflection data acquired across the northern Ecuador–southwest Colombia margin, *J. Geophys. Res.*, *109*, B11103, doi:10.1029/2004JB003060.

Comte, D., M. Pardo, L. Dorbath, C. Dorbath, H. Haessler, L. Rivera, A. Cisternas, and L. Ponce (1994), Determination of seismogenic interplate contact zone and crustal seismicity around Antofagasta, northern Chile, *Geophys. J. Int.*, *116*, 553–561, doi:10.1111/j.1365-246X.1994.tb03279.x.

Delouis, B., M. Pardo, D. Legrand, and T. Monfret (2009), The Mw 7.7 Tocopilla earthquake of 14 November 2007 at the southern edge of the northern Chile seismic gap: Rupture in the deep part of the coupled plate interface, *Bull. Seismol. Soc. Am.*, *99*(1), 87–94, doi:10.1785/0120080192.

DeMets, C., R. G. Gordon, D. F. Argus, and S. Stein (1994), Effect of recent revisions to the geomagnetic reversal time scale on current plate motions, *Geophys. Res. Lett.*, *21*, 2191–2194, doi:10.1029/94GL02118.

Dorbath, L., A. Cisternas, and C. Dorbath (1990), Assessment of the size of large and great historical earthquakes in Peru, *Bull. Seismol. Soc. Am.*, *80*(3), 551–576.

Dragert, H., K. Wang, and T. S. James (2001), A silent slip event on the deeper Cascadia subduction interface, *Science*, *292*, 1525–1528, doi:10.1126/science.1060152.

Engdhal, E., R. van der Hilst, and R. Buland (1998), Global teleseismic earthquake relocation with improved travel times and procedures for depth determination, *Bull. Seismol. Soc. Am.*, *88*, 722–743.

Farr, T. G., and M. Kobrick (2000), Shuttle Radar Topography Mission produces a wealth of data, *Eos Trans. AGU*, *81*(48), 583.

Freymueller, J. T., S. C. Cohen, and H. J. Fletcher (2000), Spatial variations in present-day deformation, Kenai Peninsula, Alaska, and their implications, *J. Geophys. Res.*, *105*, 8079–8101, doi:10.1029/1999JB900388.

Gagnon, K., C. D. Chadwell, and E. Norabuena (2005), Measuring the onset of locking in the Peru-Chile trench with GPS and acoustic measurements, *Nature*, *434*(7030), 205–208, doi:10.1038/nature03412.

Giovanni, M. K., S. L. Beck, and L. Wagner (2002), The June 23, 2001 Peru earthquake and the southern Peru subduction zone, *Geophys. Res. Lett.*, *29*(21), 2018, doi:10.1029/2002GL015774.

Hashimoto, C., A. Noda, T. Sagiya, and M. Matsu'ura (2009), Interplate seismogenic zones along the Kuril–Japan trench inferred from GPS data inversion, *Nat. Geosci.*, *2*, 141–144, doi:10.1038/ngeo1421.

Haskell, N. (1964), Total energy and energy spectral density of elastic wave radiation from propagating faults, *Bull. Seismol. Soc. Am.*, *56*, 1811–1842.

Heki, K., and Y. Tamura (1997), Short term afterslip in the 1994 Sanriku-Haruka-Oki earthquake, *Geophys. Res. Lett.*, *24*(24), 3285–3288, doi:10.1029/97GL03316.

Hetland, E. A., M. Simons, and E. M. Dunham (2010), Post-seismic and interseismic fault creep I: Model description, *Geophys. J. Int.*, *181*, 81–98, doi:10.1111/j.1365-246X.2010.04522.x.

Hindle, D., J. Kley, E. Klosko, S. Stein, T. Dixon, and E. Norabuena (2002), Consistency of geologic and geodetic displacements during Andean orogenesis, *Geophys. Res. Lett.*, *29*(8), 1188, doi:10.1029/2001GL013757.

Hirose, H., K. Hirahara, F. Kimata, N. Fujii, and S. Miyazaki (1999), A slow thrust slip event following the two 1996 Hyuganada earthquakes beneath the Bungo Channel, southwest Japan, *Geophys. Res. Lett.*, *26*(21), 3237–3240, doi:10.1029/1999GL010999.

Hsu, Y.-J., M. Simons, J. P. Avouac, K. Sieh, J. Galetzka, M. Chlieh, Y. Bock, D. H. Natawidjaja, and L. Prawirodirdjo (2006), Frictional afterslip following the Mw 8.7, 2005 Nias-Simeuleu earthquake, Sumatra, *Science*, *312*(5782), 1921–1926, doi:10.1126/science.1126960.

Hu, Y., K. Wang, J. He, J. Klotz, and G. Khazaradze (2004), Three-dimensional viscoelastic finite element model for postseismic deformation of the great 1960 Chile earthquake, *J. Geophys. Res.*, *109*, B12403, doi:10.1029/2004JB003163.

Hyndman, R. D., M. Yamano, and D. A. Oleskevich (1997), The seismogenic zone of subduction thrust faults, *Isl. Arc*, *6*(3), 244–260, doi:10.1111/j.1440-1738.1997.tb00175.x.

Ji, C., D. Wald, and D. V. Helmberger (2002), Source description of the 1999 Hector Mine, California earthquake, part I: Wavelet domain inversion theory and resolution analysis, *Bull. Seismol. Soc. Am.*, *92*(4), 1192–1207, doi:10.1785/0120000916.

Johnson, K. M., and P. Segall (2004), Viscoelastic earthquake cycle models with deep stress-driven creep along the San Andreas fault system, *J. Geophys. Res.*, *109*, B10403, doi:10.1029/2004JB003096.

Kanamori, H., and K. C. McNally (1982), Variable rupture mode of the subduction zone along the Ecuador-Colombia coast, *Bull. Seismol. Soc. Am.*, *72*(4), 1241–1253.

Kanda, R. V. S., and M. Simons (2010), An elastic plate model for interseismic deformation in subduction zones, *J. Geophys. Res.*, *115*, B03405, doi:10.1029/2009JB006611.

Kaneko, Y., J.-P. Avouac, and N. Lapusta (2010), Towards inferring earthquake patterns from geodetic observations of interseismic coupling, *Nat. Geosci.*, *3*, 363–369, doi:10.1038/ngeo843.

Kendrick, E., M. Bevis, R. J. Smalley, and B. Brooks (2001), An integrated crustal velocity field for the central Andes, *Geochem. Geophys. Geosyst.*, *2*(11), 1066, doi:10.1029/2001GC000191.

Kendrick, E., M. Bevis, J. R. Smalley, B. Brooks, R. B. Vargas, E. Lauria, and L. P. Souto Fortes (2003), The Nazca-South America Euler vector and its rate of change, *J. South Am. Earth Sci.*, *16*(2), 125–131, doi:10.1016/S0895-9811(1003)00028-00022.

Khazaradze, G., and J. Klotz (2003), Short and long-term effects of GPS measured crustal deformation rates along the south-central Andes, *J. Geophys. Res.*, *108*(B6), 2289, doi:10.1029/2002JB001879.

Khazaradze, G., K. Wang, J. Klotz, Y. Hu, and J. He (2002), Prolonged post-seismic deformation of the 1960 great Chile earthquake and implications for mantle rheology, *Geophys. Res. Lett.*, *29*(22), 2050, doi:10.1029/2002GL015986.

Kley, J., and C. R. Monaldi (1998), Tectonic shortening and crustal thickness in the Central Andes: How good is the correlation?, *Geology*, *26*(8), 723–726, doi:10.1130/0091-7613(1998)026<0723:TSACTI>2.3.CO;2.

Konca, A. O., et al. (2008), Partial rupture of a locked patch of the Sumatra megathrust during the 2007 earthquake sequence, *Nature*, *456*, 631–635, doi:10.1038/nature07572.

Lamb, S. (2000), Active deformation in the Bolivian Andes, South America, *J. Geophys. Res.*, *105*, 25,627–25,653.

Langer, C. J., and W. Spence (1995), The 1974 Peru earthquake series, *Seismol. Soc. Am.*, *85*(3), 665–687.

Liu, Y., and J. R. Rice (2007), Spontaneous and triggered aseismic deformation transients in a subduction fault model, *J. Geophys. Res.*, *112*, B09404, doi:10.1029/2007JB004930.

Llenos, A. L., and J. J. McGuire (2007), Influence of fore-arc structure on the extent of great subduction zone earthquakes, *J. Geophys. Res.*, *112*, B09301, doi:10.1029/2007JB004944.

Loveless, J. P., and B. J. Meade (2010), Geodetic imaging of plate motions, fault slip rates, and partitioning of deformation in Japan, *J. Geophys. Res.*, *115*, B02410, doi:10.1029/2008JB006248.

Loveless, J. P., R. W. Allmendinger, M. E. Pritchard, J. L. Garroway, and G. González (2009), Surface cracks record long-term seismic segmentation of the Andean margin, *Geology*, *37*, 23–26, doi:10.1130/G25170A.1.

Lowry, A. R., K. M. Larson, V. Kostoglodov, and R. Bilham (2001), Transient fault slip in Guerrero, southern Mexico, *Geophys. Res. Lett.*, *28*, 3753–3756, doi:10.1029/2001GL013238.

Massonnet, D., M. Rossi, C. Carmona, F. Adragna, G. Peltzer, K. Feigl, and T. Rabaute (1993), The displacement field of the Landers earthquake mapped by radar interferometry, *Nature*, *364*(6433), 138–142, doi:10.1038/364138a0.

McQuarrie, N., J. B. Barnes, and T. A. Ehlers (2008), Geometric, kinematic and erosional history of the central Andean Plateau, *Tectonics*, *27*, TC3007, doi:10.1029/2006TC002054.

Melnick, D., B. Bookhagen, M. R. Strecker, and H. Echtler (2009), Segmentation of megathrust rupture zones from forearc deformation patterns over hundreds to millions of years, Arauco Peninsula, *J. Geophys. Res.*, *114*, B01407, doi:10.1029/2008JB005788.

Miyazaki, S., J. J. McGuire, and P. Segall (2003), A transient subduction zone slip episode in southwest Japan observed by the nationwide GPS array, *J. Geophys. Res.*, *108*(B2), 2087, doi:10.1029/2001JB000456.

Moreno, M., M. Rosenau, and O. Oncken (2010), 2010 Maule earthquake slip correlates with pre-seismic locking of Andean subduction zone, *Nature*, *467*, 198–202, doi:10.1038/nature09349.

Motagh, M., R. Wang, T. R. Walter, R. Brgmann, E. Fielding, J. Anderssohn, and J. Zschau (2008), Coseismic slip model of the 2007 August Pisco earthquake (Peru) as constrained by wide swath radar observations, *Geophys. J. Int.*, *174*(3), 842–848, doi:10.1111/j.1365-1246X.2008.03852.x.

Norabuena, E., L. Leffler-Griffin, A. Mao, T. Dixon, S. Stein, I. S. Sacks, L. Ocola, and M. Ellis (1998), Space geodetic observations of Nazca-South America convergence across the central Andes, *Science*, *279*(5349), 358–362, doi:10.1126/science.1279.5349.1358.

Oleskevich, D. A., R. D. Hyndman, and K. Wang (1999), The updip and downdip limit to great subduction earthquakes: Thermal and structural models of Cascadia, South Alaska, SW Japan and Chile, *J. Geophys. Res.*, *104*(B7), 14,965–14,991, doi:10.1029/1999JB900060.

Oncken, O., D. Hindle, J. Kley, K. Elger, P. Victor, and K. Schemmann (2006), Deformation of the Central Andean upper plate system—Facts, fiction, and constraints for plateau models, in *The Andes: Active Subduction Orogeny*, *Frontiers in Earth Sci. Ser.*, vol. 1, edited by O. Oncken et al., pp. 3–28, Springer, Berlin.

Perfettini, H., and J.-P. Ampuero (2008), Dynamics of a velocity strengthening fault region: Implications for slow earthquakes and postseismic slip, *J. Geophys. Res.*, *113*, B09411, doi:10.1029/2007JB005398.

Perfettini, H., and J. P. Avouac (2004), Stress transfer and strain rate variations during the seismic cycle, *J. Geophys. Res.*, *109*, B06402, doi:10.1029/2003JB002917.

Perfettini, H., and J. P. Avouac (2007), Modeling afterslip and aftershocks following the 1992 Landers earthquake, *J. Geophys. Res.*, *112*, B07409, doi:10.1029/2006JB004399.

Perfettini, H., et al. (2010), Aseismic and seismic slip on the Megathrust offshore southern Peru revealed by geodetic strain before and after the Mw8.0, 2007 Pisco earthquake, *Nature*, *465*, 78–81, doi:10.1038/nature09062.

Peyrat, S., R. Madariaga, E. Buforn, J. Campos, G. Asch, and J. P. Vilotte (2010), Kinematic rupture process of the 2007 Tocopilla earthquake and its main aftershocks from teleseismic and strong motion data, *Geophys. J. Int.*, *182*, 1411–1430, doi:10.1111/j.1365-1246X.2010.04685.x.

Pritchard, M. E., and E. J. Fielding (2008), A study of the 2006 and 2007 earthquake sequence of Pisco, Peru, with InSAR and teleseismic data, *Geophys. Res. Lett.*, *35*, L09308, doi:10.1029/2008GL033374.

Pritchard, M. E., and M. Simons (2006), An aseismic slip pulse in northern Chile and along-strike variations in seismogenic behavior, *J. Geophys. Res.*, *111*, B08405, doi:10.1029/2006JB004258.

Pritchard, M. E., E. O. Norabuena, C. Ji, R. Boroschek, D. Comte, M. Simons, T. H. Dixon, and P. A. Rosen (2007), Geodetic, teleseismic, and strong motion constraints on slip from recent southern Peru subduction zone earthquakes, *J. Geophys. Res.*, *112*, B03307, doi:10.1029/2006JB004294.

Robinson, D. P., S. Das, and A. B. Watts (2006), Earthquake rupture stalled by a subducting fracture zone, *Science*, *312*, 1203–1205, doi:10.1126/science.1125771.

Salichon, J., B. Delouis, P. Lundgren, D. Giardini, M. Costantini, and P. Rosen (2003), Joint inversion of broadband teleseismic and interferometric synthetic aperture radar (InSAR) data for the slip history of the Mw = 7.7, Nazca ridge (Peru) earthquake of 12 November 1996, *J. Geophys. Res.*, *108*(B2), 2085, doi:10.1029/2001JB000913.

Savage, J. C. (1983), A dislocation model of strain accumulation and release at a subduction zone, *J. Geophys. Res.*, *88*, 4984–4996, doi:10.1029/JB088iB06p04984.

Scholz, C. H. (1998), Earthquakes and friction laws, *Nature*, *391*, 37–42, doi:10.1038/34097.

Sella, G. F., T. H. Dixon, and A. L. Mao (2002), REVEL: A model for Recent plate velocities from space geodesy, *J. Geophys. Res.*, *107*(B4), 2081, doi:10.1029/2000JB000033.

Silgado, E. (1978), *Historia de los sismos más notables ocurridos en el Perú, 1513–1974*, 131 pp., Inst. Geol. Minero del Peru, Lima.

Simons, M., et al. (2011), The 2011 magnitude 9.0 Tohoku-Oki earthquake: Mosaicking the megathrust from seconds to centuries, *Science*, *332*(6036), 1421–1425, doi:10.1126/science.1206731.

Sladen, A., H. Tavera, M. Simons, J.-P. Avouac, A. O. Konca, H. Perfettini, L. Audin, E. J. Fielding, and F. Ortega (2010), Source Model of the 2007 Mw 8.0 Pisco, Peru earthquake: Implications for seismogenic behavior of subduction megathrusts, *J. Geophys. Res.*, *115*, B02405, doi:10.1029/2009JB006429.

Song, T.-R. A., and M. Simons (2003), Large trench-parallel gravity variations predict seismogenic behavior in subduction zones, *Science*, *301*, 630–633, doi:10.1126/science.1085557.

Spence, W., C. Mendoza, E. R. Engdahl, G. L. Choy, and E. Norabuena (1999), Seismic subduction of the Nazca Ridge as shown by the 1996–97 Peru earthquakes, *Pure Appl. Geophys.*, *154*, 753–776, doi:10.1007/s000240050251.

Swenson, J. L., and S. L. Beck (1999), Source characteristics of the 12 November 1996 Mw 7.7 Peru subduction zone earthquake, *Pure Appl. Geophys.*, *154*(3), 731–751, doi:10.1007/s000240050250.

Tavera, H., and I. Bernal (2008), The Pisco (Peru) earthquake of 15 August 2007, *Seismol. Res. Lett.*, *79*(4), 510–515, doi:10.1785/gssrl.1779.1784.1510.

Tavera, H., E. Buforn, I. Bernal, Y. Antayhua, and L. Vilacapoma (2002), The Arequipa (Peru) earthquake of June 23, 2001, *J. Seismol.*, *6*(2), 279–283, doi:10.1023/A:1015698621075.

Thatcher, W. (1990), Order and diversity in the modes of circum-Pacific earthquake recurrence, *J. Geophys. Res.*, *95*(B3), 2609–2623, doi:10.1029/JB095iB03p02609.

Tichelaar, B. W., and L. J. Ruff (1991), Seismic coupling along the Chilean subduction zone, *J. Geophys. Res.*, *96*, 11,997–12,022.

Vergne, J., R. Cattin, and J.-P. Avouac (2001), On the use of dislocations to model interseismic strain and stress build-up at intracontinental thrust faults, *Geophys. J. Int.*, *147*, 155–162, doi:10.1046/j.1365-246X.2001.00524.x.

Victor, P., M. Sobiesiak, S. Nielsen, J. Glodny, and O. Oncken (2011), Long-term persistence of subduction earthquake segment boundaries: Evidence from Mejillones Peninsula, northern Chile, *J. Geophys. Res.*, *116*, B02402, doi:10.1029/2010JB007771.

Vigny, C., A. Rudloff, J. C. Ruegg, R. Madariaga, J. Campos, and M. Alvarez (2009), Upper plate deformation measured by GPS in the Coquimbo gap, Chile, *Phys. Earth Planet. Inter.*, *175*(1–2), 86–95, doi:10.1016/j.pepi.2008.1002.1013.

Walker, C. F. (2008), *Shaky Colonialism: The 1746 Earthquake-Tsunami in Lima, Peru, and Its Long Aftermath*, 280 pp., Duke Univ. Press, Durham, N. C.

Wallace, L. M., J. Beavan, R. McCaffrey, and D. Darby (2004), Subduction zone coupling and tectonic block rotations in the North Island, New Zealand, *J. Geophys. Res.*, *109*, B12406, doi:10.1029/2004JB003241.

Wang, K., R. Wells, S. Mazzotti, R. D. Hyndman, and T. Sagiya (2003), A revised dislocation model of interseismic deformation of the Cascadia subduction zone, *J. Geophys. Res.*, *108*(B1), 2026, doi:10.1029/2001JB001227.

Wang, K., Y. Hu, M. Bevis, E. Kendrick, R. J. Smalley, R. B. Vargas, and E. Lauría (2007), Crustal motion in the zone of the 1960 Chile earthquake: Detangling earthquake-cycle deformation and forearc-sliver translation, *Geochem. Geophys. Geosyst.*, *8*, Q10010, doi:10.1029/2007GC001721.

Wells, R. E., R. J. Blakely, Y. Sugiyama, D. W. Scholl, and P. A. Dinterman (2003), Basin-centered asperities in great subduction zone earthquakes: A

link between slip, subsidence, and subduction erosion?, *J. Geophys. Res.*, *108*(B10), 2507, doi:10.1029/2002JB002072.

Xie, X., and Z. X. Yao (1989), A generalized reflection-transmission coefficient matrix method to calculate static displacement field of a dislocation source in a stratified half space, *Chin. J. Geophys.*, *32*, 191–205.

Yoshioka, S., T. Mikumo, V. Kostoglodov, K. M. Larson, A. R. Lowry, and S. Singh (2004), Interplate coupling and a recent aseismic slow slip event in the Guerrero seismic gap of the Mexican subduction zone, as deduced from GPS data inversion using a Bayesian information criterion, *Phys. Earth Planet. Inter.*, *146*, 513–530, doi:10.1016/j.pepi.2004.1005.1006.

J.-P. Avouac, Tectonics Observatory, California Institute of Technology, Pasadena, CA 91125, USA.

F. Bondoux, S. Bonvalot, G. Gabalda, and D. Remy, Géosciences Environnement Toulouse, IRD UR 234, CNRS UMR 5563, Université de Toulouse, Observatoire Midi-Pyrénées, 14 av. E. Belin, F-31400 Toulouse, France.

M. Chlieh and J.-M. Nocquet, Géoazur, IRD UR 082, CNRS UMR 6526, Université de Nice Sophia-Antipolis, Observatoire de la Côte d'Azur, 250 rue A. Einstein, F-06560 Valbonne, France. (chlieh@geoazur.unice.fr)

H. Perfettini, Institut des Sciences de la Terre, IRD UR 219, CNRS UMR 5275, Université Joseph Fourier, Observatoire des Sciences de l'Univers de Grenoble, BP 53, F-38041 Grenoble CEDEX 9, France.

F. Rolandone, Institut des Sciences de la Terre de Paris, CNRS UMR 7193, Université Pierre et Marie Curie, 4 place Jussieu, F-75005 Paris, France.

H. Tavera, Instituto Geofisico del Peru, Calle Badajoz #169 Mayorazgo IV Etapa–Ate, Lima, Peru.